Heliyon

Received:
8 July 2018
Revised:
5 November 2018
Accepted:
2 January 2019

Cite as: Misbah Ijaz, Muhammad Ayub. Nonlinear convective stratified flow of Maxwell nanofluid with activation energy. Heliyon 5 (2019) e01121. doi: 10.1016/j.heliyon.2019.e01121

Nonlinear convective stratified flow of Maxwell nanofluid with activation energy

Misbah Ijaz*, Muhammad Ayub

Department of Mathematics, Quaid-I-Azam University 45320, Islamabad 44000, Pakistan

* Corresponding author.

E-mail address: misbahijaz@math.qau.edu.pk (M. Ijaz).

Abstract

The aim of present article is to explore the novel aspects of activation energy in nonlinearly convective flow of Maxwell nanofluid driven by nonlinearly stretched inclined cylinder. Generalized forms of Fourier's and Fick's law are utilized through Cattaneo-Christov double diffusion scheme. Maxwell nanomaterial model is used to describe the significant slip mechanism namely known as Brownian and thermophoresis diffusions. Features of double stratification, non-uniform heat generation/absorption, binary chemical reaction and activation energy are considered for present flow problem. Modified Arrhenius formula for activation energy is implemented. The resulting nonlinear system is cracked for series solutions via homotopy technique. Effects of different flow parameters on temperature, nanoparticle volume concentration and velocity fields are examined through graphs and tables. Numerical computations are performed for local Nusselt and Sherwood numbers. Our analysis reveals that nanoparticle concentration is directly proportional to the chemical reaction with activation energy. Moreover stratification variables diminish the temperature and concentration. It is also noticed that higher estimation of Deborah number declines the velocity profile of Maxwell fluid. Numerical outcomes are compared with previous published results and found to be in good agreement for limiting cases of the evolving parameters.

Keywords: Applied mathematics, Computational mathematics, Mechanics

https://doi.org/10.1016/j.heliyon.2019.e01121

1. Introduction

Non-Newtonian flows have attained considerable significance due to its applications in the fields of applied science and engineering. Viscoelastic fluid is a subclass of non-Newtonian fluid that exhibit both viscous and memory effect after the removal of applied stress. Some common viscoelastic fluids are flour dough, egg white, polymers, bitumen, blood and paints. Viscoelastic impacts are primarily essential when there are abrupt changes in the strain rate as during contractions/expansions, pulsating flows and during start-up flow or stoppage. Maxwell model designates the viscoelastic effects in terms of stress relaxation time that is the time required for the elastic effects to decay. Viscoelastic materials are used in automobile bumpers, on computer drives to protect from mechanical shock, in helmets (the foam padding inside), in wrestling mats, in shoe insoles to reduce impact transmitted to a person's skeleton. Synthetic viscoelastic materials can be injected directly into an osteoarthritic knee, enveloping cartilage-deficient joints and acting as a lubricant and shock absorber. Abel et al. [1] performed numerical computations for steady flow of Maxwell fluid in view of isothermal stretched surface. Hayat et al. [2] analyzed the problem of Maxwell fluid with effects of melting heat transfer via homotopic technique. Thermally stratified flow of Maxwell fluid with radiation effect is explored by Hayat et al. [3]. Mustafa et al. [4] presented numerical analysis of Maxwell nanofluid over an exponentially stretched plate. Radiative flow of Maxwell fluid in addition to non-uniform heat source and slip effects is inspected by Zheng et al. [5]. Hayat et al. [6] investigated nonlinear convective flow of Maxwell fluid with Cattaneo-Christov double diffusion by variable thickness sheet.

Mechanism of heat and mass transport occurs naturally due to non-equilibrium state of temperature and concentration within the medium or between different objects. This process has great number of industrial and engineering applications like paper production, artificial fibers, nuclear reactor cooling system, chemical waste migration, wire drawing, extrusion processes, hot rolling distillation towers and so on. In past, remarkable efforts have been accomplished to discover system of heat and mass transport by employing renowned Fourier's law of heat theory [7] and Fick's law of mass diffusion [8]. Energy expression through Fourier's law is of parabolic type. That indicates that initial disturbance is promptly transmitted/sensed by the medium under consideration. This fact of heat transfer is identified as "paradox of heat conduction". Later, Cattaneo [9] added a thermal relaxation time factor in heat expression to resolve this paradox of heat. Christov [10] additionally revised Cattaneo [9] theory by replacing time derivative with Oldroyd upper convective derivative. This modification is acknowledged by Cattaneo-Christov theory. The stability in thermal state in Brinkman permeable medium by Cattaneo-Christov flux model is offered by Haddad [11]. Hayat et al. [12] presented a comparative study of second grade and elastico-viscous fluids in view of Cattaneo-Christov heat flux theory.

https://doi.org/10.1016/j.heliyon.2019.e01121

Waqas et al. [13] examined heat transfer through Cattaneo-Christov heat flux model for generalized Burgers fluid over a stretched surface. Hayat et al. [14] studied Jeffrey fluid flow subject to Cattaneo-Christov double-diffusion over a stretched surface. Some more recent research has been stated at [15, 16, 17, 18, 19, 20, 21, 22, 23].

The influence of heat generation/absorption on heat mechanism is another noteworthy aspect in view of numerous physical problems. Heat distribution is directly changed by heat generation/absorption in the fluid that consequently influenced the rate of particle deposition in the medium/system like nuclear reactors, electronic devices and semiconductors. Heat source/sink might be viewed as constant, space or temperature based. In the present situation, we will examine non-uniform heat source/sink that depends on space and temperature. Abo-Eldahab and El-Aziz [24] discussed the effect of non-uniform heat source for the case of viscous fluid only. Abel et al. [25] considered boundary layer flow of non-Newtonian over a stretched sheet in view of non-uniform heat source and frictional heating. Abel and Mahesha [26] studied the heat transfer of a non-Newtonian viscoelastic fluid over a flat sheet in account of non-uniform heat source, variable thermal conductivity and thermal radiation. Greesha et al. [27] deliberated the impact of non-uniform heat source/sink for Casson fluid model. Some significant researches related to heat source/sink are presented in the investigations [28, 29, 30, 31, 32].

The mass transfer mechanism with chemical reaction and activation energy has been given marvelous attention due to its numerous applications in geothermal reservoirs, chemical engineering, thermal oil recovery, food processing and cooling of nuclear reactors. The eminent Arrhenius law (Eq. (1)) is generally of the form [33]:

$$K = B^{*}(T - T_{\infty})^{\widehat{p}} exp\left[-\frac{E_A}{k(T - T_{\infty})}\right], \tag{1}$$

In the above expression, K stands for reaction rate, E_A for activation energy and k ($=8.61 \times 10^{-5}$ eV/K) for Boltzmann constant. Here factor B^{*} defines a noticeable rise in reaction rate when temperature is enhanced. Activation energy phenomenon is frequently applicable in eminent areas such as oil reservoir engineering or geothermal. There exist few theoretical works in literature related to activation power for different flow problems. Theoretically, it is rather difficult to tackle mass transfer equation indicating the state of all involved chemical reactions in the system. According to chemical kinetic theory, this problem is over viewed by imposing the restriction of binary chemical reaction. Truesdell [34, 35] initially discovered the expression of thermochemical equation for mixture of materials. Bestman [36] examined the impact of activation energy in naturally convective flow of binary mixture through a permeable medium. Maleque [37] measured the feature of activation energy and exothermic reactions for unsteady flow of liquid past a vertical porous surface. Kandasamy et al. [38] deliberated feature of heat and mass transfer

https://doi.org/10.1016/j.heliyon.2019.e01121

along a wedge in presence of suction or injection, chemical reaction and heat source. Makinde et al. [39] analyzed unsteady convective flow with radiative heat transfer and chemical reaction over a permeable flat plate.

The main objective of the present article is to investigate the nonlinearly convective flow of Maxwell nanofluid in account of activation energy, non-uniform heat source/sink and double stratification. The flow is induced due to nonlinearly stretched surface of an inclined cylinder with thermal and solutal stratification phenomena. The novelty of problem is to investigate the Cattaneo-Christov double-diffusion model for viscoelastic fluid with additional effects of space and temperature dependent heat generation/absorption, nonlinear mixed convection and duel stratification. Brownian motion and thermophoresis are also considered. The novel binary chemical reaction model is applied to portray the impact of activation energy. Solutions of highly non-linear modeled equations are accomplished by employing homotopic technique [40, 41, 42, 43]. Behaviors of various pertinent parameters on the velocity, temperature, and concentration distributions are shown graphically. Nusselt and Sherwood numbers are computed numerically for different involved parameters.

2. Model

Here we consider nonlinear convective flow of Maxwell nanofluid over an inclined stretched cylinder of radius R_o in account of Cattaneo-Christov double-diffusion model. The cylindrical polar coordinates $(\tilde{r}, z)$ are preferred along radial and axial directions of cylinder (see Fig. 1). Flow is maintained by nonlinearly stretching velocity of the form $W_w(z) = \frac{W_o^* z^n}{L}$ with stretching rate $W_o^* > 0$. Analysis has been executed in presence of nonuniform heat source/sink, dual stratification, binary chemical reaction, nonlinear mixed convection and Arrhenius activation energy. Features of nanoparticles are also taken in the version of thermophoresis and Brownian motion. Temperature and concentration at surface of cylinder are $T_w = T_o + \frac{f_1 z}{L}$ and $C_w = C_o + \frac{f_3 z}{L}$. While ambient fluid temperature and concentration are stratified in the form $T_\infty = T_o + \frac{f_2 z}{L}$ and $C_\infty = C_o + \frac{f_4 z}{L}$ respectively. The governing equations in view of boundary layer approximation are given by Eqs. (2) and (3).

$$\frac{\partial}{\partial z}(\tilde{r}u_1) + \frac{\partial}{\partial \tilde{r}}(\tilde{r}w_1) = 0, \tag{2}$$

$$\left.\begin{aligned} w_1\frac{\partial w_1}{\partial z} + u_1\frac{\partial w_1}{\partial \tilde{r}} + \lambda_m\left(w_1^2\frac{\partial^2 w_1}{\partial z^2} + u_1^2\frac{\partial^2 w_1}{\partial \tilde{r}^2} + 2w_1u_1\frac{\partial^2 w_1}{\partial \tilde{r}\partial z}\right) &= \nu_1\frac{\partial^2 w_1}{\partial \tilde{r}^2} \\ + \frac{\tilde{g}_1}{\tilde{\rho}_f}\left[\Psi_1(T - T_\infty) + \Psi_2(T - T_\infty)^2 + \Psi_3(C - C_\infty) + \Psi_4(C - C_\infty)^2\right]\cos\phi_1, & \end{aligned}\right\} \tag{3}$$

https://doi.org/10.1016/j.heliyon.2019.e01121

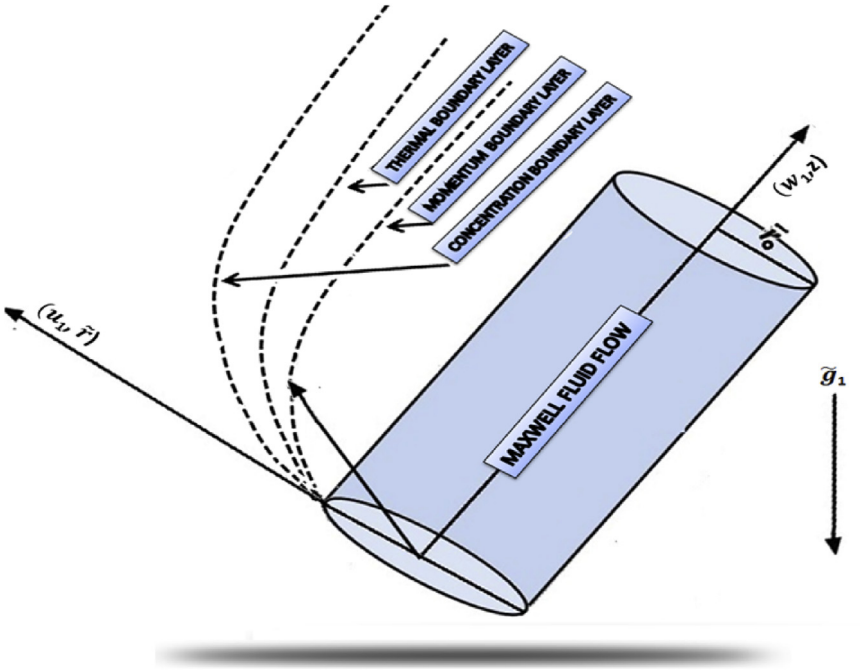

Fig. 1. Flow geometry.

here (u_1, w_1) defines the velocities in $(\tilde{r}, z)$ directions respectively, λ_m stands for fluid relaxation time, $\nu_1\left(\left(=\frac{\mu}{\tilde{\rho}}\right)_f\right)$ for kinematic viscosity, ϕ_1 for angle of inclination, $\tilde{\rho}_f$ for fluid density, L for characteristic length of the cylinder, $\tilde{g}_1$ gravitational acceleration, $(\mathrm{T_o}, \mathrm{C_o})$ for reference temperature and concentration, (Ψ_1, Ψ_2) for linear and nonlinear thermal expansion coefficients, (Ψ_3, Ψ_4) for linear and nonlinear solutal expansion coefficients, respectively. Cattaneo-Christove double diffusive scheme [44] is expressed in Eqs. (4) and (5).

$$\mathbf{q}_1 + \psi_e\left[\frac{\partial \mathbf{q}_1}{\partial t} + \boldsymbol{V}.\nabla_1\mathbf{q}_1 - \mathbf{q}_1.\nabla_1\boldsymbol{V} + (\nabla_1.\boldsymbol{V})\mathbf{q}_1\right] = -\tilde{k}_1\nabla_1\mathrm{T}, \tag{4}$$

$$\mathbf{j}_1 + \psi_c\left[\frac{\partial \mathbf{j}_1}{\partial t} + \boldsymbol{V}.\nabla_1\mathbf{j}_1 - \mathbf{j}_1.\nabla_1\boldsymbol{V} + (\nabla_1.\boldsymbol{V})\mathbf{j}_1\right] = -D_B\nabla_1\mathrm{C}, \tag{5}$$

in above equations D_B stands for Brownian diffusion coefficient, $\boldsymbol{q}_1$ for heat flux, $\tilde{k}_1$ for thermal conductivity, $\mathbf{j}_1$ for mass flux, (ψ_e, ψ_c) for relaxation time of heat and mass fluxes respectively. Standard Fourier and Fick's laws are obtained when $\psi_e = \psi_c = 0$. For steady $\left(\frac{\partial \mathbf{q}_1}{\partial t} = \frac{\partial \mathbf{j}_1}{\partial t} = 0\right)$ and incompressible fluid $(\nabla_1.\boldsymbol{V} = 0)$, Cattaneo-Christove double diffusion expression are given by Eqs. (6) and (7)

https://doi.org/10.1016/j.heliyon.2019.e01121

$$\mathbf{q}_1 + \psi_e[\boldsymbol{V}.\nabla_1\mathbf{q}_1 - \mathbf{q}_1.\nabla_1\boldsymbol{V} + (\nabla_1.\boldsymbol{V})\mathbf{q}_1] = -\tilde{k}_1\nabla_1\mathrm{T}, \tag{6}$$

$$\mathbf{j}_1 + \psi_e[\boldsymbol{V}.\nabla_1\mathbf{j}_1 - \mathbf{j}_1.\nabla_1\boldsymbol{V} + (\nabla_1.\boldsymbol{V})\mathbf{j}_1] = -D_B\nabla_1\mathrm{C}, \tag{7}$$

The energy (Eq. (8)) and concentration (Eq. (9)) expressions in view of non-uniform heat source/sink, activation energy, Brownian motion and thermophoresis are

$$\left.\begin{aligned} u_1\frac{\partial T}{\partial\tilde{r}} + w_1\frac{\partial T}{\partial z} + \psi_e\widehat{\Omega}_e = \frac{\tilde{k}_1}{(\rho\mathrm{C}_p)_f}\frac{1}{\tilde{r}}\frac{\partial}{\partial\tilde{r}}\left(\tilde{r}\frac{\partial T}{\partial\tilde{r}}\right) + \frac{\widehat{q}_m}{(\rho\mathrm{C}_p)_f} \\ +\tau_1\mathrm{D}_B\left(\frac{\partial\mathrm{C}}{\partial\tilde{r}}\frac{\partial T}{\partial\tilde{r}}\right) + \frac{\tau_1\mathrm{D}_T}{T_\infty}\left(\frac{\partial T}{\partial\tilde{r}}\right)^2, \end{aligned}\right\} \tag{8}$$

$$\left.\begin{aligned} u_1\frac{\partial\mathrm{C}}{\partial\tilde{r}} + w_1\frac{\partial\mathrm{C}}{\partial z} + \psi_e\widehat{\Omega}_c = \frac{\mathrm{D}_B}{\tilde{r}}\frac{\partial}{\partial\tilde{r}}\left(\tilde{r}\frac{\partial\mathrm{C}}{\partial\tilde{r}}\right) + \frac{\mathrm{D}_T}{T_\infty}\frac{1}{\tilde{r}}\frac{\partial}{\partial\tilde{r}}\left(\tilde{r}\frac{\partial T}{\partial\tilde{r}}\right) - \breve{k}(\mathrm{C}-\mathrm{C}_\infty) \\ -(\mathrm{C}_w-\mathrm{C}_o)\widehat{K}_r^2\left(\frac{T}{T_\infty}\right)^{\widehat{p}}exp\left[-\frac{A_o}{T\dot{k}_1}\right], \end{aligned}\right\} \tag{9}$$

The boundary conditions (Eq. (10)) and Cattaneo-Christove expression $\widehat{\Omega}_e$ and $\widehat{\Omega}_c$ are defined in Eqs. (11) and (12)

$$\left.\begin{aligned} w_1 = \frac{W_o^*z^n}{L}, u_1 = 0, T = T_w = T_o + \frac{f_1 z}{L}, C = \mathrm{C}_w = \mathrm{C}_o + \frac{f_3 z}{L} at\ \tilde{r} = R_o, \\ w_1 \to 0, T \to T_\infty = T_o + \frac{f_2 z}{L}, C \to \mathrm{C}_\infty = \mathrm{C}_o + \frac{f_4 z}{L} as\ \tilde{r} \to \infty, \end{aligned}\right\} \tag{10}$$

$$\widehat{\Omega}_e = u_1^2\frac{\partial^2 T}{\partial\tilde{r}^2} + w_1^2\frac{\partial^2 T}{\partial z^2} + \frac{\partial T}{\partial\tilde{r}}\left(w_1\frac{\partial u_1}{\partial z} + u_1\frac{\partial u_1}{\partial\tilde{r}}\right) + \left(w_1\frac{\partial w_1}{\partial z} + u_1\frac{\partial w_1}{\partial\tilde{r}}\right)\frac{\partial T}{\partial z} + 2w_1u_1\frac{\partial^2 w_1}{\partial\tilde{r}\partial z}, \tag{11}$$

$$\widehat{\Omega}_c = u_1^2\frac{\partial^2\mathrm{C}}{\partial\tilde{r}^2} + w_1^2\frac{\partial^2\mathrm{C}}{\partial z^2} + \frac{\partial\mathrm{C}}{\partial\tilde{r}}\left(w_1\frac{\partial u_1}{\partial z} + u_1\frac{\partial u_1}{\partial\tilde{r}}\right) + \left(w_1\frac{\partial w_1}{\partial z} + u_1\frac{\partial w_1}{\partial\tilde{r}}\right)\frac{\partial\mathrm{C}}{\partial z} + 2w_1u_1\frac{\partial^2 w_1}{\partial\tilde{r}\partial z}, \tag{12}$$

The formulation of non-uniform heat source/sink $\widehat{q}_m$ [45] is given by Eq. (13)

$$\widehat{q}_m = \frac{W_w(z)\tilde{k}_1}{z\nu_1}\left[\tilde{S}_1(T_w - T_o)\frac{\partial\mathrm{F}}{\partial\Lambda_1} + \tilde{S}_2(T - T_\infty)\right], \tag{13}$$

where $\tilde{S}_1$ and $\tilde{S}_2$ defines coefficients of space and temperature dependent heat source/sink, respectively. The positive case of $\tilde{S}_1$ and $\tilde{S}_2$ denote internal heat generation, while negative values of represent internal heat absorption. Here $\tau_1\left(=\frac{(\rho\mathrm{C}_p)_p}{(\rho\mathrm{C}_p)_f}\right)$ designates for specific heat ratio, D_T for themophoretic diffusion

https://doi.org/10.1016/j.heliyon.2019.e01121

coefficient and $(C_p)_f$ for specific heat respectively. The expression $\widehat{K}_r^2\left(\frac{T}{T_\infty}\right)^{\widehat{p}} exp\left[-\frac{A_o}{T\ddot{k}_1}\right]$ is Arrhenius function with $\ddot{k}_1(=8.61\times10^{-5})$ as Boltzmann constant, $\widehat{K}_r^2$ reaction rate parameter and $\widehat{p}\in(-1,1)$ fitted rate constant respectively.

According to the transformations mentioned in Eq. (14)

$$\left.\begin{aligned}
&\Lambda_1=\sqrt{\frac{(n+1)}{2}\frac{W_o^* z^{n-1}}{L\nu_1}}\left(\frac{\tilde{r}^2-R_o^2}{2R_o}\right),\ \Psi(\Lambda_1)=\sqrt{\frac{2}{(n+1)}\frac{\nu_1 W_o^* z^{n+1}}{L}}\mathrm{F}(\Lambda_1),\\
&w_1(\Lambda_1)=\frac{W_o^* z^n}{L}\mathrm{F}'(\Lambda_1),\quad \Theta_1(\Lambda_1)=\frac{T-T_\infty}{T_w-T_o},\quad \Phi_1(\Lambda_1)=\frac{\mathrm{C}-\mathrm{C}_\infty}{\mathrm{C}_w-\mathrm{C}_o},\\
&u_1(\Lambda_1)=\frac{R_o}{\tilde{r}}\sqrt{\frac{(n+1)}{2}\frac{\nu_1 W_o^* z^{n-1}}{L}}\left[\mathrm{F}(\Lambda_1)+\Lambda_1\left(\frac{n-1}{n+1}\right)\mathrm{F}'(\Lambda_1)\right],
\end{aligned}\right\}\tag{14}$$

The flow expressions in view of above mentioned transformations are presented by Eqs. (15), (16), and (17) along with transformed boundary conditions (Eq. (18))

$$\left.\begin{aligned}
&(1+2\widehat{\gamma}\Lambda_1)\mathrm{F}'''-\frac{2n}{n+1}\mathrm{F}'^2+\frac{2}{n+1}\xi_1\left[\left(1+\tilde{\beta}_t\Theta_1\right)\Theta_1+\tilde{N}_1\left(1+\tilde{\beta}_c\Phi_1\right)\Phi_1\right]\cos\phi_1\\
&+\mathrm{F}\mathrm{F}''+\widehat{\gamma}\mathrm{F}''-\xi\left[\begin{array}{l}\frac{(n+1)}{2}\left(\mathrm{F}'''\mathrm{F}^2+\widehat{\gamma}(1+2\widehat{\gamma}\Lambda_1)^{-1}\left(\mathrm{F}+\Lambda_1\frac{n-1}{n+1}\mathrm{F}'\right)^2\right)\mathrm{F}''\\ -(3n-1)\mathrm{F}''\mathrm{F}'\mathrm{F}+\frac{2n(n-1)}{n+1}\mathrm{F}'^3-\left(\frac{n-1}{2}\right)\Lambda_1\mathrm{F}'^2\mathrm{F}''\end{array}\right]=0,
\end{aligned}\right\}\tag{15}$$

$$\left.\begin{aligned}
&(1+2\widehat{\gamma}\Lambda_1)\left[\Theta_1''+\mathrm{Pr}\tilde{\mathrm{N}}_\mathrm{b}\left(\Theta_1'\Phi_1'+\frac{\tilde{\mathrm{N}}_\mathrm{t}}{\tilde{\mathrm{N}}_\mathrm{b}}\Theta_1'^2+Ec\mathrm{F}''^2\right)\right]+2\widehat{\gamma}\Theta_1'+Pr\mathrm{F}\Theta_1'\\
&-PrU_e\left[\frac{n+1}{2}\left(\Theta_1''\mathrm{F}^2-\mathrm{F}\mathrm{F}'\Theta_1'\right)+\frac{2}{n+1}\left(\tilde{P}_1+\Theta_1\right)\left(\mathrm{n}\mathrm{F}'^2-\frac{n+1}{2}\mathrm{F}\mathrm{F}''\right)\right]\\
&+\frac{2}{n+1}\left(\tilde{S}_1\mathrm{F}'+\tilde{S}_2\Theta_1\right)-\frac{2}{n+1}Pr\left(\tilde{P}_1+\Theta_1\right)\mathrm{F}'=0,
\end{aligned}\right\}\tag{16}$$

https://doi.org/10.1016/j.heliyon.2019.e01121

$$\left.\begin{aligned}&(1+2\widehat{\gamma}\Lambda_1)\Phi_1''+2\widehat{\gamma}\Phi_1'+ScF\Phi_1'+\frac{\tilde{N}_t}{\tilde{N}_b}\left[(1+2\widehat{\gamma}\Lambda_1)\Theta_1''+2\widehat{\gamma}\Theta_1'\right]-\\&ScU_c\left[\left(\frac{n+1}{2}\right)\left(\Phi_1''F^2-FF'\Phi_1'\right)+\frac{2}{n+1}\left(\tilde{P}_2+\Phi_1\right)\left(nF'^2-\frac{n+1}{2}FF''\right)\right]-\\&\frac{2}{n+1}Sc\left(\left(\tilde{P}_2+\Phi_1\right)F'+\gamma_1\Phi_1\right)-ScU_3\left(1+\tilde{\delta}_1\Theta_1\right)^{\widehat{p}}exp\left[-\frac{E_o}{1+\tilde{\delta}_1\Theta_1}\right]=0,\end{aligned}\right\}\tag{17}$$

$$\left.\begin{aligned}F'(0)=1,\quad F(0)=0,\quad \Theta_1(0)=1-\tilde{P}_1,\quad \Phi_1(0)=1-\tilde{P}_2,\\F'(\infty)\to 0,\quad \Theta_1(\infty)\to 0,\quad \Phi_1(\infty)\to 0,\end{aligned}\right\}\tag{18}$$

where ξ stands for Deborah number in terms of relaxation time, $\tilde{\beta}_c$ non-linear mixed convection parameter for concentration, $\tilde{N}_1$ for ratio of concentration to thermal buoyancy forces, E_o for activation energy parameter, Gr Grashof number for temperature, U_c for non-dimensional solutal relaxation time, Grashof number for concentration, Pr for Prandtl number, $\tilde{N}_t$ thermophoresis parameter, U_3 for reaction rate constant, Sc Schmidt number, γ_1 for chemical reaction, $\tilde{\delta}_1$ temperature difference, $\tilde{P}_2$ for solutal stratification parameter, $\widehat{\gamma}$ for curvature parameter, $\tilde{\beta}_t$ for non-linear convection parameter for temperature, $\tilde{P}_1$ for thermal stratification parameter, ξ_1 for mixed convection parameter, U_e for non-dimensional thermal relaxation time, Ec for Eckert number and $\tilde{N}_b$ for Brownian motion parameter, respectively.

These dimensionless quantities are defined in Eq. (19)

$$\left.\begin{aligned}&\xi=\frac{\lambda_m W_o^* z^{n-1}}{L},\ \tilde{\beta}_c=\frac{\Psi(C_w-C_o)}{\Psi_3},\ \tilde{N}_1=\frac{\tilde{G}r}{Gr}=\frac{\Psi_3(C_w-C_o)}{\Psi_1(T_w-T_o)},\\&E_o=\frac{A_o}{T_\infty \ddot{k}_1},\ Y_c=\frac{W_o^*\psi_c z^{n-1}}{L},\ Gr=\frac{\tilde{g}_1\Psi_1(T_w-T_o)z^3}{\nu_1^2},\ \gamma_1=\frac{\breve{k}L}{W_o^* z^{n-1}},\\&Pr=\frac{(\mu C_p)_f}{\tilde{k}_1},\ \tilde{G}r=\frac{\tilde{g}_1\Psi_3(C_w-C_o)z^3}{\nu_1^2},\ Y_3=\frac{L\widehat{K}_r^2}{W_o^* z^{n-1}},\ Sc=\frac{\nu_1}{D_B},\\&\tilde{N}_t=\frac{\tau_1 D_T(T_w-T_o)}{T_\infty \nu_1},\ \tilde{\delta}_1=\frac{(T_w-T_o)}{T_\infty},\ \tilde{P}_2=\frac{f_4}{f_3},\ \tilde{\beta}_t=\frac{\Psi_2(T_w-T_o)}{\Psi_1},\\&\widehat{\gamma}=\sqrt{\frac{2}{n+1}\frac{L\nu_1}{R_o^2 W_o^*}z^{-\frac{n-1}{2}}},\tilde{P}_1=\frac{f_2}{f_1},\xi_1=\frac{Gr}{Re_z^2}=\frac{L^2\Psi_1(T_w-T_o)\tilde{g}_1}{W_o^{*2}z^{2n-1}},\\&Ec=\frac{W_w^2}{C_p(T_w-T_o)},\ Y_e=\frac{W_o^*\psi_e z^{n-1}}{L},\ \tilde{N}_b=\frac{\tau_1 D_B(C_w-C_o)}{\nu_1},\end{aligned}\right\}\tag{19}$$

Skin friction coefficient $\tilde{C}_F$, Nusselt $\tilde{N}u_z$ and Sherwood numbers $\tilde{S}h_z$ are given by Eq. (20)

https://doi.org/10.1016/j.heliyon.2019.e01121

$$\tilde{\mathrm{C}}_{\mathrm{F}}=\frac{2\tau_w}{\tilde{\rho}W_w^2},\ \tilde{N}u_z=\frac{zq_w}{\tilde{k}_1(T_w-T_o)},\ \tilde{S}h_z=\frac{zj_w}{\mathrm{D}_B(\mathrm{C}_w-\mathrm{C}_o)}, \tag{20}$$

where wall shear stress, wall heat and mass flux are defined in Eq. (21)

$$\tau_w=\left|(1+\xi)\frac{\partial w_1}{\partial\tilde{r}}\right|_{\tilde{r}=R_o},\quad q_w=-\left|\tilde{k}_1\frac{\partial T}{\partial\tilde{r}}\right|_{\tilde{r}=R_o},\quad j_w=-\left|\mathrm{D}_B\frac{\partial \mathrm{C}}{\partial\tilde{r}}\right|_{\tilde{r}=R_o}, \tag{21}$$

Using Eqs. (14) and (21) in Eq. (20), we obtain Eq. (22)

$$\left.\begin{aligned}\frac{1}{2}\tilde{\mathrm{C}}_{\mathrm{F}}(Re_z)^{\frac{1}{2}}&=\left(\frac{n+1}{2}\right)^{\frac{1}{2}}(1+\xi)\mathrm{F}''(0),\\ \tilde{N}u_z(Re_z)^{-\frac{1}{2}}&=-\left(\frac{n+1}{2}\right)^{\frac{1}{2}}\Theta_1'(0),\\ \tilde{S}h_z(Re_z)^{-\frac{1}{2}}&=-\left(\frac{n+1}{2}\right)^{\frac{1}{2}}\Phi_1'(0),\end{aligned}\right\} \tag{22}$$

in which local Reynold number is defined by Eq. (23)

$$Re_z=\frac{z^{n+1}W_o^*}{L\nu_1}. \tag{23}$$

3. Methodology

The selected initial approximations $(\mathrm{F}^{\circ}(\Lambda_1),\Theta_1^{\circ}(\Lambda_1),\Phi_1^{\circ}(\Lambda_1))$ and linear operators $(\pounds_{\mathrm{F}},\pounds_{\Theta_1},\pounds_{\Phi_1})$ are presented by Eqs. (24) and (25)

$$\left.\begin{aligned}\mathrm{F}^{\circ}(\Lambda_1)=1-\exp(-\Lambda_1),\quad \Theta_1^{\circ}(\Lambda_1)=\left(1-\tilde{P}_1\right)\exp(-\Lambda_1),\\ \Phi_1^{\circ}(\Lambda_1)=\left(1-\tilde{P}_2\right)\exp(-\Lambda_1),\end{aligned}\right\} \tag{24}$$

$$\pounds_{\mathrm{F}}[\mathrm{F}]=\mathrm{F}'''-\mathrm{F}',\quad \pounds_{\Theta_1}[\Theta_1]=\Theta_1''-\Theta_1,\quad \pounds_{\Phi_1}[\chi_1]=\Theta_1''-\Phi_1, \tag{25}$$

with associated properties (Eq. (26))

$$\left.\begin{aligned}&\pounds_{\mathrm{F}}[\widehat{q}_1exp(-\Lambda_1)+\widehat{q}_2+\widehat{q}_3exp(\Lambda_1)]=0,\\ &\pounds_{\Theta_1}[\widehat{q}_4exp(-\Lambda_1)+\widehat{q}_5exp(\Lambda_1)]=0,\\ &\pounds_{\Phi_1}[\widehat{q}_6exp(-\Lambda_1)+\widehat{q}_7exp(\Lambda_1)]=0.\end{aligned}\right\} \tag{26}$$

According to procedure (see Ref. [46]), the general solutions (Eq. (27)) interms of special solutions $(\widehat{\mathrm{F}}_m(\Lambda_1),\ \widehat{\Theta}_{1m}(\Lambda_1),\ \widehat{\Phi}_{1m}(\Lambda_1))$ are

https://doi.org/10.1016/j.heliyon.2019.e01121

$$\left.\begin{aligned} \mathrm{F}_m(\Lambda_1) &= \widehat{\mathrm{F}}_m + \widehat{q}_1 exp(-\Lambda_1) + \widehat{q}_2 + \widehat{q}_3 exp(\Lambda_1), \\ \Theta_{1m}(\Lambda_1) &= \widehat{\Theta}_{1m} + \widehat{q}_4 exp(-\Lambda_1) + \widehat{q}_5 exp(\Lambda_1), \\ \Phi_{1m}(\Lambda_1) &= \widehat{\Phi}_{1m} + \widehat{q}_6 exp(-\Lambda_1) + \widehat{q}_7 exp(\Lambda_1). \end{aligned}\right\} \tag{27}$$

where $\widehat{q}_j (j = 1 - 7)$ are the arbitrary constants given by Eq. (28)

$$\left.\begin{aligned} &\widehat{q}_1 = -\widehat{\mathrm{F}}_m(0) + \frac{\partial \widehat{\mathrm{F}}_m}{\partial \Lambda_1}\bigg|_{\Lambda_1=0}, \ \widehat{q}_2 = \frac{\partial \widehat{\mathrm{F}}_m}{\partial \Lambda_1}\bigg|_{\Lambda_1=0}, \ \widehat{q}_4 = -\widehat{\Theta}_{1m}(\Lambda_1)\big|_{\Lambda_1=0} \\ &\widehat{q}_6 = -\widehat{\Phi}_{1m}(\Lambda_1)\big|_{\Lambda_1=0}, \qquad \widehat{q}_3 = \widehat{q}_5 = \widehat{q}_7 = 0. \end{aligned}\right\} \tag{28}$$

4. Analysis

The nonlinear flow problem is examined through homotopic technique for convergent solution. In this method, auxiliary parameters are involved which provide great freedom to adjust the convergence region for velocity $\mathrm{F}''(0)$, temperature $\Theta_1'(0)$ and concentration $\Phi_1'(0)$ profiles. Therefore, h − curves of 20^{th} order approximation are shown in Fig. 2. It is noticed that permissible values of $\mathrm{h_F}$, h_{Θ_1} and h_{Φ_1} lie in the ranges $(-1.7 \leq \mathrm{h_F} \leq -0.7)$, $(-1.6 \leq \mathrm{h}_{\Theta_1} \leq -0.9)$ and $(-1.5 \leq \mathrm{h}_\Gamma \leq -0.8)$. Convergence of the derived solutions is studied from Table 1 to highlight 26^{th}, 30^{th} and 20^{th} order of approximations for $\mathrm{F}''(0)$, $\Theta_1'(0)$ and $\Phi_1'(0)$ respectively. Fixed values of emerging parameters for present analysis are $\widehat{\gamma} = \xi = \tilde{\mathrm{P}}_1 = U_c = 0.3$, $\mathrm{Pr} = \mathrm{Sc} = 1.5$, $\tilde{\beta}_t = \tilde{\mathrm{P}}_2 = \tilde{\mathrm{S}}_1 = \tilde{\beta}_c = U_e = \tilde{\mathrm{S}}_2 = 0.2$, $U_3 = \tilde{\mathrm{N}}_1 =$

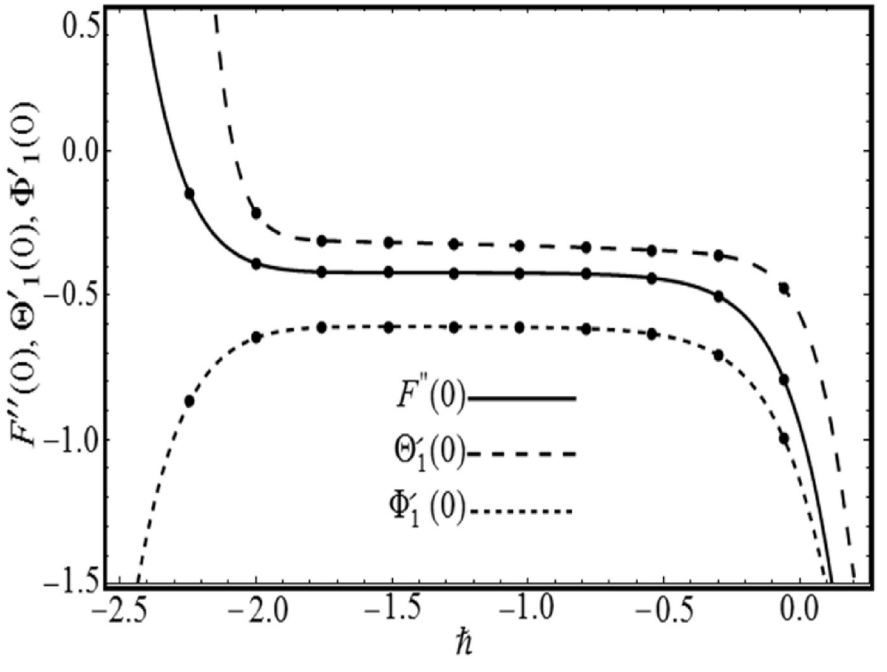

Fig. 2. h_{F}, h_{Θ_1} and h_{Φ_1} − *curves*.

https://doi.org/10.1016/j.heliyon.2019.e01121

Table 1. Numerical convergence of $F''(0)$, $\Theta_1'(0)$ and $\Phi_1'(0)$ when $\widehat{\gamma} = \xi = \tilde{P}_1 = U_c = 0.3$, $Pr = Sc = 1.5$, $\tilde{\beta}_t = \tilde{P}_2 = \tilde{S}_1 = \tilde{\beta}_c = U_e = \tilde{S}_2 = 0.2$, $U_3 = \tilde{N}_1 = E_o = \tilde{\delta}_1 = 1.0$, $p = \tilde{N}_t = n = \xi_1 = \tilde{N}_b = 0.5$, $\gamma_1 = 0.9$, Ec $= 1.0$ ***and*** $\phi_1 = \frac{\pi}{4}$.

Approximation	$-F''(0)$	$-\Theta_1'(0)$	$-\Phi_1'(0)$
1	0.38642	0.30745	0.58247
5	0.39123	0.32012	0.58479
11	0.39627	0.31426	0.58640
16	0.40878	0.32562	0.58718
20	0.41403	0.32766	0.58956
26	0.42891	0.33412	0.58956
30	0.42891	0.33694	0.58956
36	0.42891	0.33694	0.58956
42	0.42891	0.33694	0.58956

$E_o = \tilde{\delta}_1 = 1.0$, $p = \tilde{N}_t = n = \xi_1 = \tilde{N}_b = 0.5$, $\gamma_1 = 0.9$, $Ec = 1.0$ and $\phi_1 = \frac{\pi}{4}$. Table 2 is constructed for numerical values of local Nusselt Nu_z and Sherwood Sh_z numbers for diverse emerging parameters. It is noticed that larger values of U_e, Pr and $\tilde{P}_2$ corresponds to the enhancement of Nusselt number however it diminishes for greater values of $\tilde{S}_1$, $\tilde{N}_t$, $\tilde{P}_1$ and U_c. It is perceived that Sherwood number rises with the increase in U_e, $\tilde{N}_b$, $\tilde{P}_2$, Pr and $\tilde{S}_1$ while it declines when $\tilde{P}_1$ and $\tilde{N}_t$ are enhanced. Here negative signs of Nusselt and Sherwood numbers characterize the transfer of heat and mass from cylindrical surface to the fluid (i.e., normal to the surface). Tables 3 and 4 are computed to compare numerical results of $F''(0)$ and $\Theta_1'(0)$ with published results. It is perceived that present results are in good match with the previous solutions.

5. Results and discussion

In this section, we will examine in detail the role of various flow variables on velocity $F'(\Lambda_1)$, temperature $\Theta_1'(\Lambda_1)$, concentration $\Phi_1'(\Lambda_1)$, heat transfer rate and mass transfer Nusselt number in graphical and tabulated frame. Figs.3, 4, 5, 6, and 7 are revealed to show the influence of $\widehat{\gamma}$, ξ, $\tilde{\beta}_t$, $\tilde{\beta}_c$ *and* ϕ_1 on $F'(\Lambda 1)$. Velocity profile decreases near the surface of cylinder while it enhances away from the surface. Fig. 3 shows the feature of curvature parameter $\widehat{\gamma}$ on $F'(\Lambda_1)$. Velocity profile vanishes asymptotically at some large values of. It is also prominent that boundary layer thickness increases. For greater estimation of, the radius of cylinder gradually decreases. So contact surface area of cylinder with the fluid decreases, which offers less resistance to the fluid motion. Therefore, $F'(\Lambda_1)$ increases. Impacts of Deborah number ξ on $F'(\Lambda_1)$ are presented in Fig. 4. It is observed that velocity profile

https://doi.org/10.1016/j.heliyon.2019.e01121

Table 2. Numerical values of $\tilde{N}u_z(Re_z)^{-\frac{1}{2}}$ and $\tilde{S}h_z(Re_z)^{-\frac{1}{2}}$ when $\gamma_1 = 0.9$, $\widehat{\gamma} = \xi = 0.3$, $U_3 = \tilde{N}_1 = E_o = \tilde{\delta}_1 = Ec = 1.0$, $Sc = 1.5$, $\tilde{\beta}_t = \tilde{\beta}_c = 0.2$, $n = \xi_1 = p = 0.5$ *and* $\phi_1 = \frac{\pi}{4}$.

Pr	$\tilde{N}_b$	$\tilde{N}_t$	$\tilde{P}_1$	$\tilde{P}_2$	U_c	U_e	$\tilde{S}_1$	$-\left(\frac{n+1}{2}\right)^{\frac{1}{2}}\Theta_1'(0)$	$-\left(\frac{n+1}{2}\right)^{\frac{1}{2}}\Phi_1'(0)$
0.6	0.5	0.5	0.3	0.2	0.3	0.2	0.2	0.63743	0.58893
1.4								0.85856	0.75205
2.0								1.01772	1.00130
1.5	0.1	0.5	0.3	0.2	0.3	0.2	0.2	0.80632	0.05884
	0.6							0.78427	0.87407
	0.8							0.73593	0.98916
1.5	0.5	0.1	0.3	0.2	0.3	0.2	0.2	0.86094	0.93704
1.5	0.5	0.1	0.3	0.2	0.3	0.2	0.2	0.86094	0.93704
		0.6						0.77561	0.49833
		0.8						0.70283	0.12053
1.5	0.5	0.5	0.0	0.2	0.3	0.2	0.2	0.86719	0.87640
			0.3					0.83011	0.82077
			0.5					0.77059	0.76344
1.5	0.5	0.5	0.3	0.0	0.3	0.2	0.2	0.75056	1.27534
				0.3				0.77575	1.34103
				0.5				0.79540	0.84569
1.5	0.5	0.5	0.3	0.2	0.1	0.2	0.2	0.88566	0.86745
					0.4			0.88539	0.87342
					0.5			0.87520	0.89011
1.5	0.5	0.5	0.3	0.2	0.3	0.1	0.2	0.76876	0.85878
						0.4		0.78456	0.87453
						0.5		0.79348	0.88324
1.5	0.5	0.5	0.3	0.2	0.3	0.2	0.1	0.85432	0.95759
							0.3	0.81672	0.98432
							0.5	0.76043	1.21434

declines for greater values of ξ. In fact, higher values of ξ correspond to an enhancement in relaxation time that produces more resistance to the fluid flow. Ultimately $F'(\Lambda_1)$ decreases. Variations of $\tilde{\beta}_t$ and $\tilde{\beta}_c$ on velocity distribution $F'(\Lambda_1)$ are shown in Figs. 5 and 6. For higher estimation of $\tilde{\beta}_t$, movement of fluid particle increases. In fact, for greater $\tilde{\beta}_t$ the temperature difference $(T_w - T_\infty)$ increases which is accountable for velocity enhancement. Increasing trends of velocity $F'(\Lambda_1)$ is also observed for greater $\tilde{\beta}_c$ (see Fig. 6). Fig. 7 portrays the decreasing trend of $F'(\Lambda_1)$ against an angle of inclination φ_1. Since inverse relation exist between velocity profile and an

https://doi.org/10.1016/j.heliyon.2019.e01121

Table 3. Comparative analysis of present results of $-F''(0)$ via ξ when $\widehat{\gamma} = \xi_1 = \tilde{\beta}_t = 0 = \tilde{\beta}_c = \tilde{N}_1 = \phi_1$.

ξ	Ref. [48]	Ref. [1]	Present (HAM)
0.0	0.999978	0.999962	1.00001
0.3	1.101848	1.101850	1.10196
0.6	1.150160	1.150163	1.15019
0.8	1.196690	1.196692	1.19676
1.2	1.285253	1.285257	1.28538
1.6	1.368641	1.368641	1.36867
2.0	1.447616	1.447617	1.44783

Table 4. Comparative analysis of present results of $-\Theta_1'(0)$ via n and Ec when $\Pr = 1.5$.

Ec	n	Ref. [47]	Present (HAM)
0.0	0.5	0.595277	0.59538
	1.5	0.574537	0.57457
	3.0	0.564472	0.56452
1.0	0.5	0.556623	0.55671
	1.5	0.530966	0.53085
	3.0	0.517977	0.51788

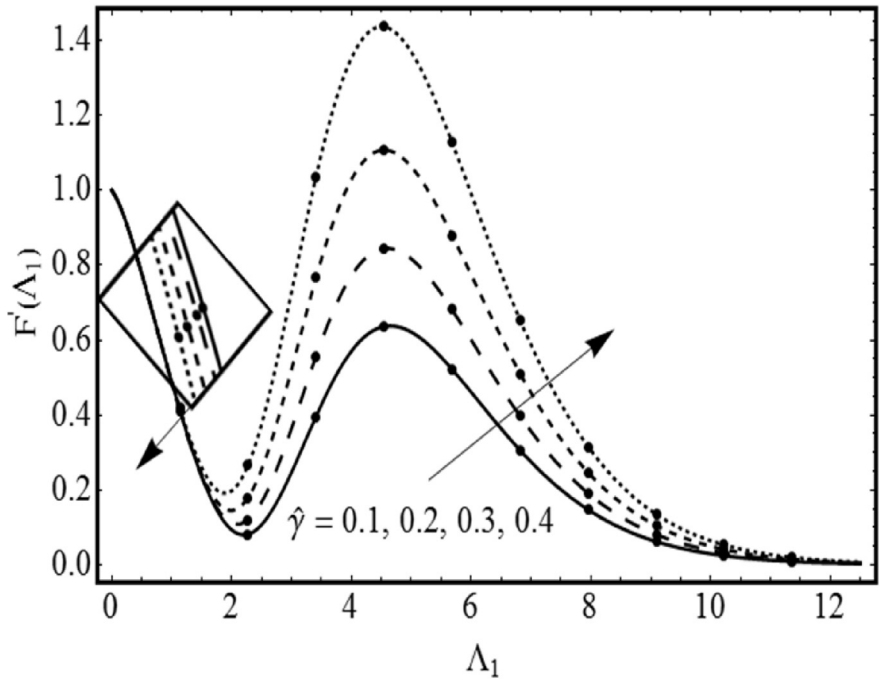

Fig. 3. Response of $F'(\Lambda_1)$ *with* $\widehat{\gamma}$.

https://doi.org/10.1016/j.heliyon.2019.e01121

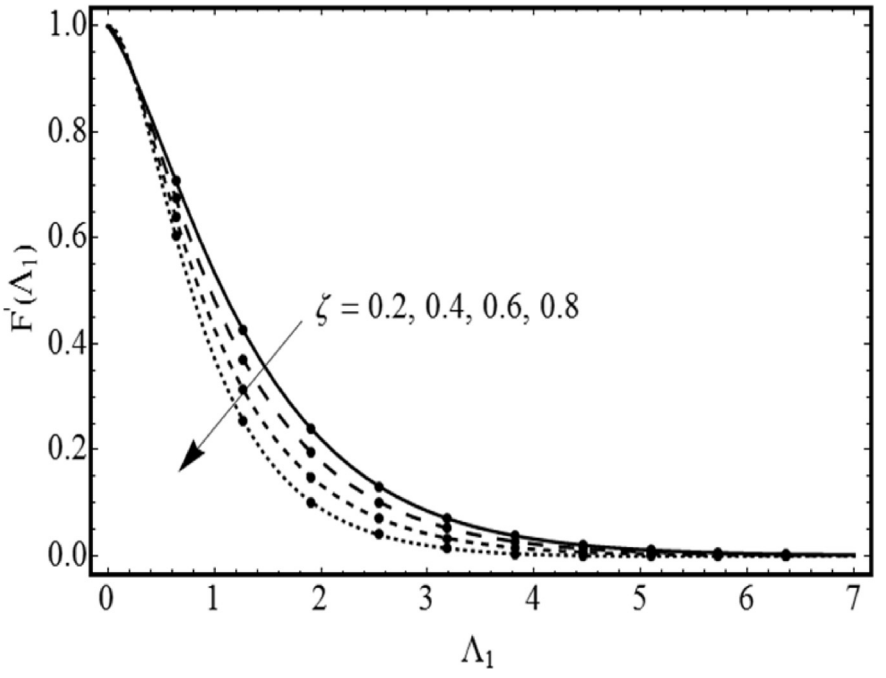

Fig. 4. Response of $F'(\Lambda_1)$ *with* ξ.

inclination φ_1. Thus, influence of gravity lessens for greater ϕ_1 about z-axis that brings decline trend in velocity field within the range of boundary layer. Figs. 8, 9, 10, 11, 12, 13, 14, and 15 are sketched to examine the temperature profile $\Theta_1(\Lambda_1)$ for different values of Behavior of temperature $\Theta_1(\Lambda_1)$ for larger estimation

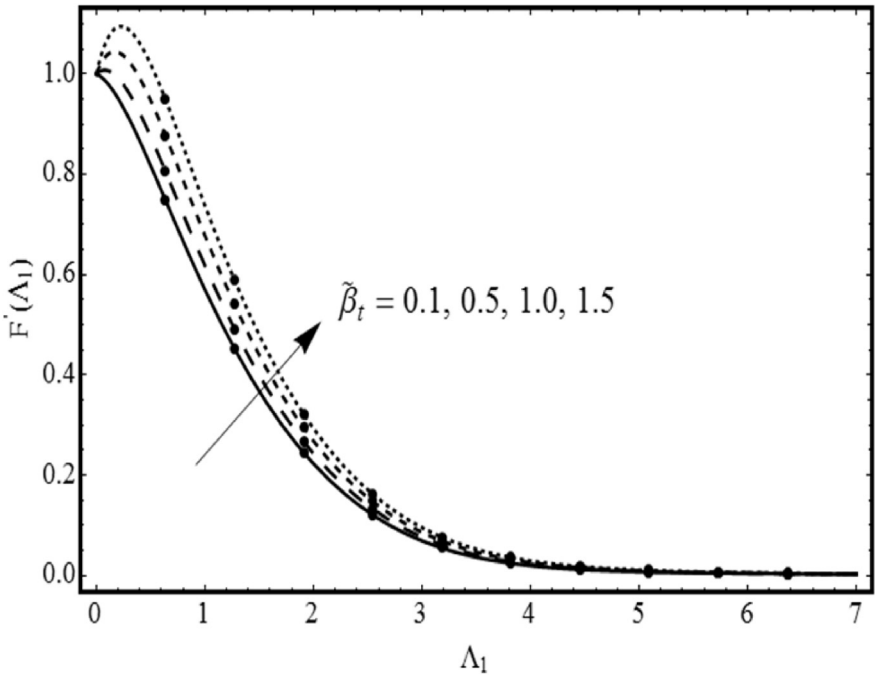

Fig. 5. Response of $F'(\Lambda_1)$ with $\tilde{\beta}_t$.

https://doi.org/10.1016/j.heliyon.2019.e01121

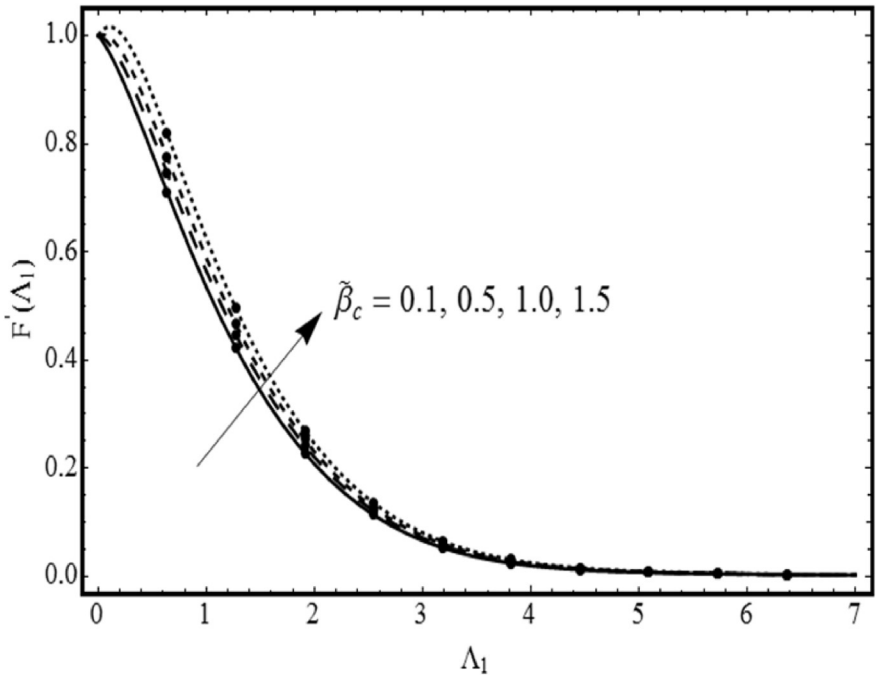

Fig. 6. Response of $F'(\Lambda_1)$ *with* $\tilde{\beta}_c$.

of Ec is displayed in Fig. 8. One can observe that temperature $\Theta_1(\Lambda_1)$ is an increasing function of Ec. For greater Ec, fluid friction generates rapidly that converts mechanical energy to thermal energy and as a result $\Theta_1(\Lambda_1)$ increases. The temperature variation against thermal relaxation parameter U_e is displayed in

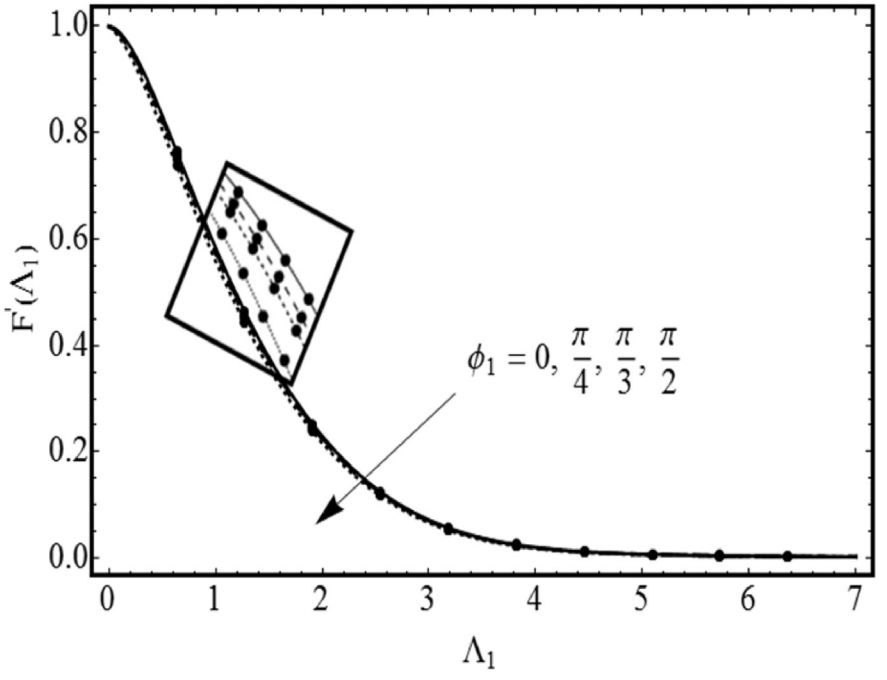

Fig. 7. Response of $F'(\Lambda_1)$ with ϕ_1.

https://doi.org/10.1016/j.heliyon.2019.e01121

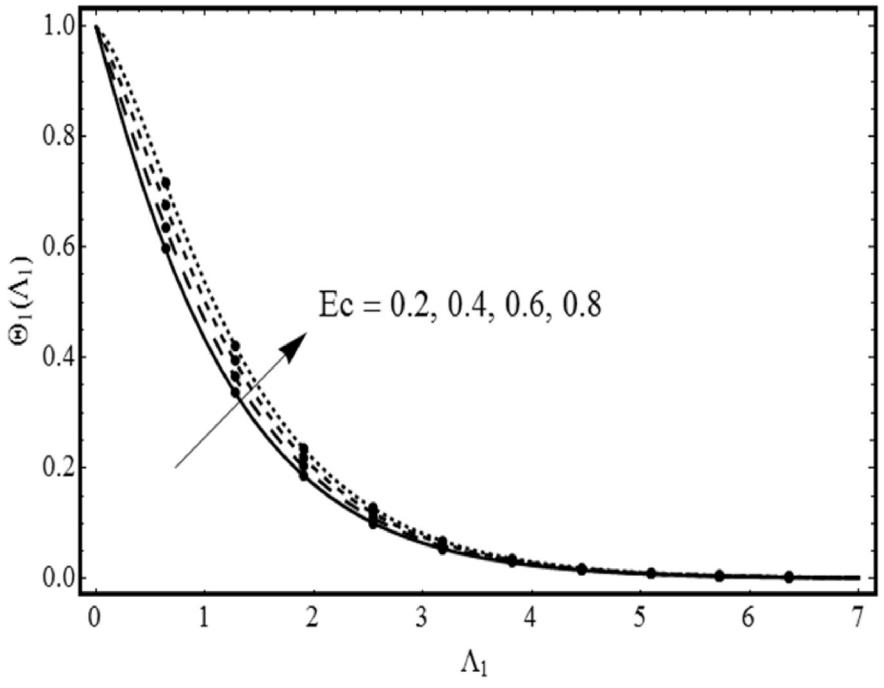

Fig. 8. Response of $F'(\Lambda_1)$ with *Ec*.

Fig. 9. Here both temperature and thermal layer thickness are reduced via greater values of U_e. Since material particle takes more time for heat transfer to its neighboring particles due to thermal relaxation enhancement. Fig. 10 reveals the effect of Brownian motion parameter $\tilde{N}_b$ on $\Theta_1(\Lambda_1)$. Increase in temperature $\Theta_1(\Lambda_1)$ and

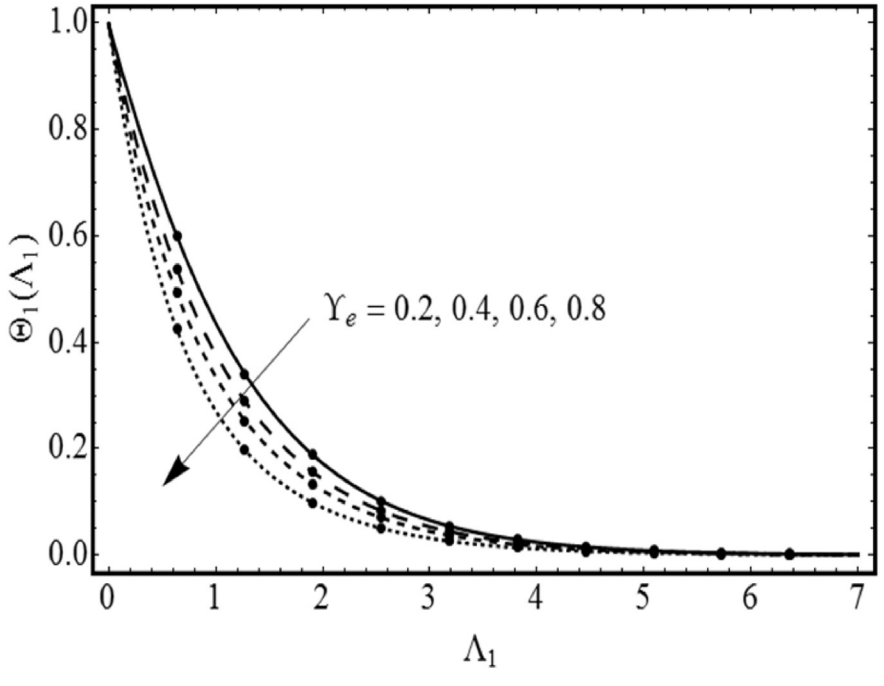

Fig. 9. Response of $\Theta_1(\Lambda_1)$ *with* U_e.

https://doi.org/10.1016/j.heliyon.2019.e01121

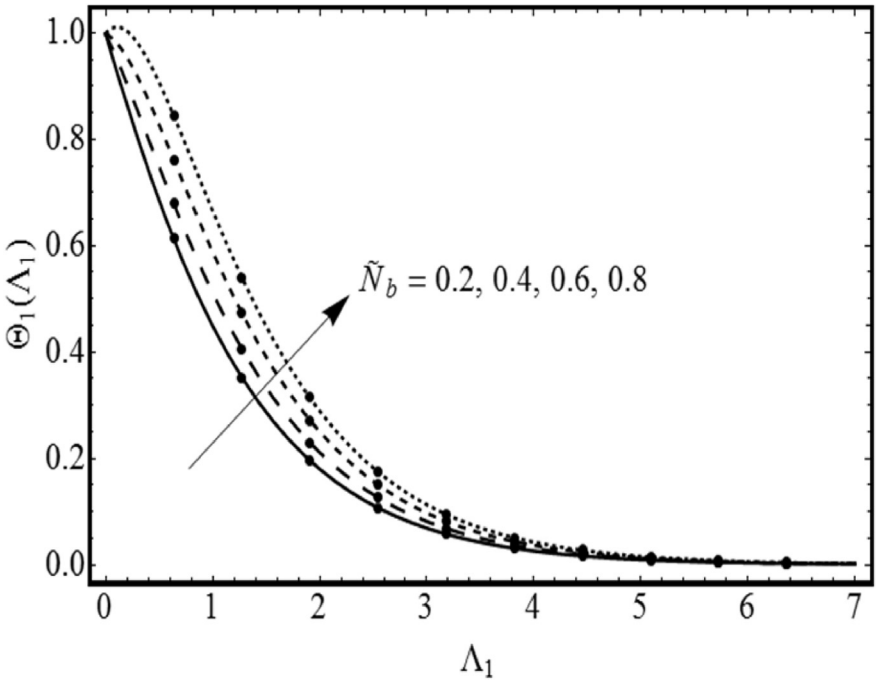

Fig. 10. Response of $\Theta_1(\Lambda_1)$ with $\tilde{N}_b$.

apposite boundary layer thickness is found for greater marks of $\tilde{N}_b$ (see Fig. 5). In fact, additional heat is generated due to random motion of liquid molecules within the frame of higher $\tilde{N}_b$. Therefore, temperature $\Theta_1(\Lambda_1)$ upsurges. Behavior of thermal stratification parameter $\tilde{P}_1$ on $\Theta_1(\Lambda_1)$ is sketched in Fig. 11. Higher estimation

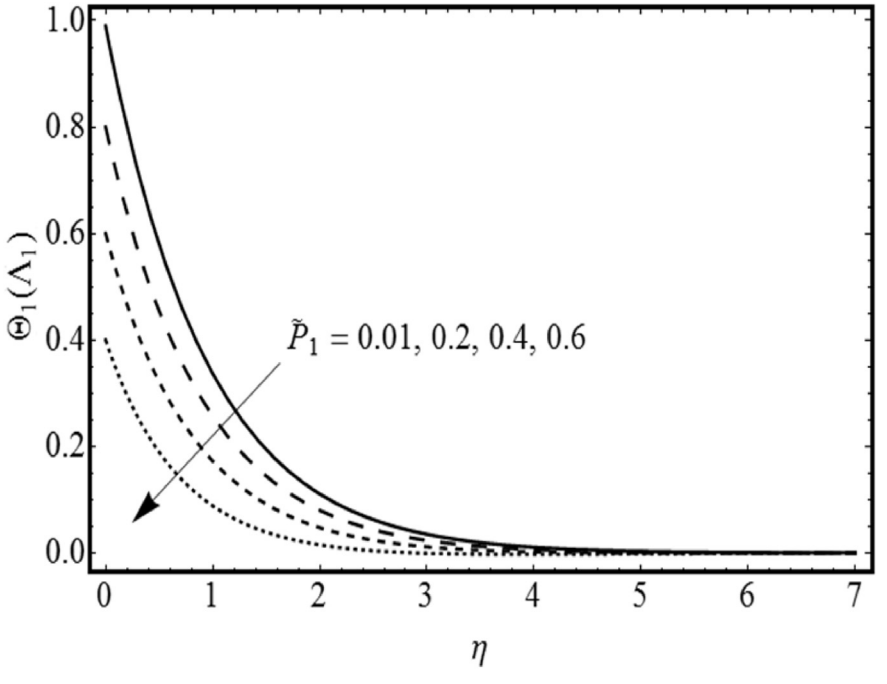

Fig. 11. Response of $\Theta_1(\Lambda_1)$ with $\tilde{P}_1$.

https://doi.org/10.1016/j.heliyon.2019.e01121

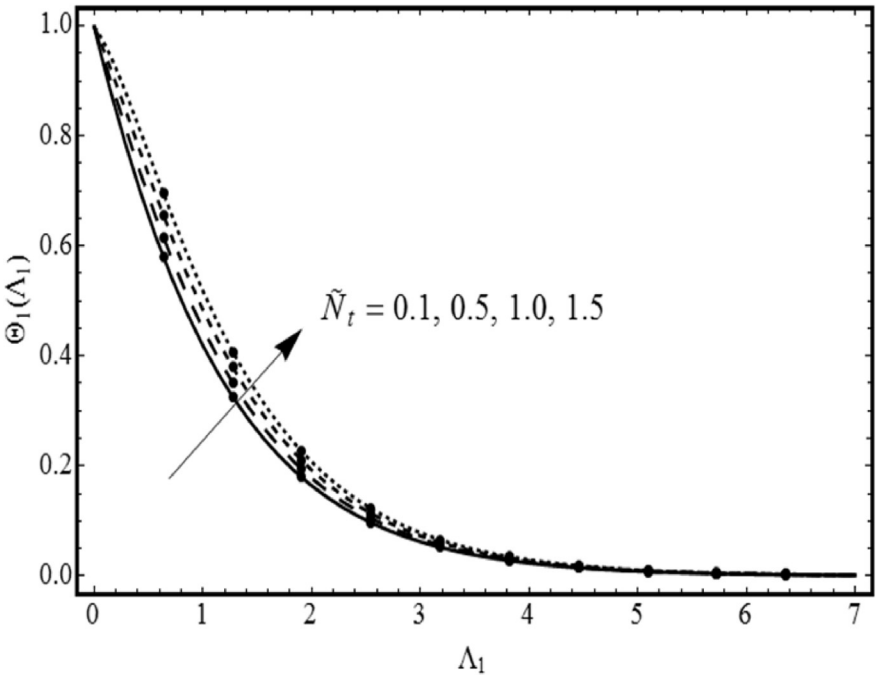

Fig. 12. Response of $\Theta_1(\Lambda_1)$ with $\tilde{N}_t$.

of $\tilde{P}_1$ reduces the temperature and thermal boundary layer thickness. This is due to the fact that the temperature difference $(T_w - T_\infty)$ gradually decreases which causes a reduction in the temperature $\Theta_1(\Lambda_1)$ profile. Variation of on temperature $\Theta_1(\Lambda_1)$ is portrayed in Fig. 12. Here $\Theta_1(\Lambda_1)$ and related boundary thickness are noticeably

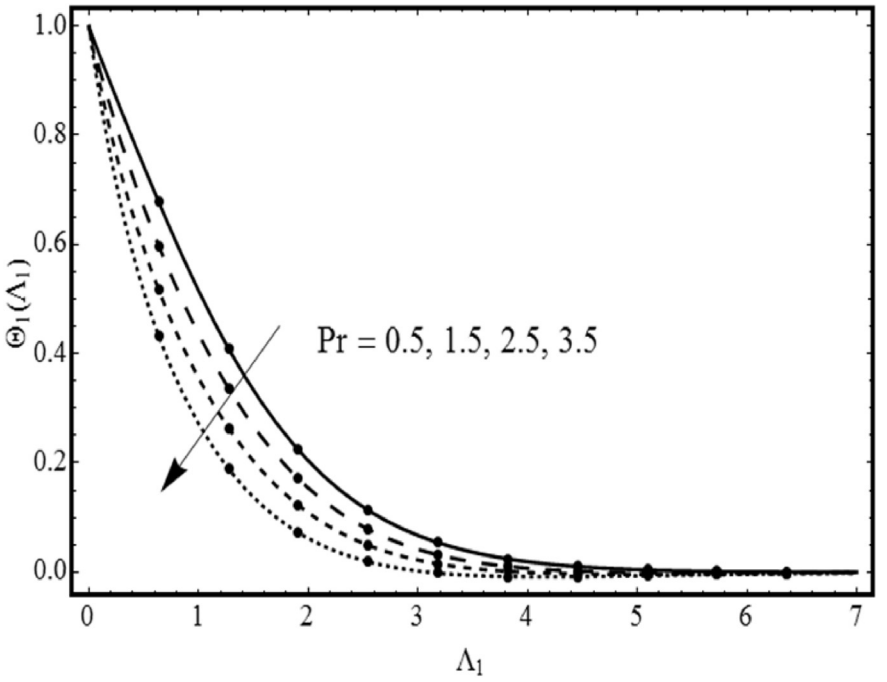

Fig. 13. Response of $\Theta_1(\Lambda_1)$ with Pr.

https://doi.org/10.1016/j.heliyon.2019.e01121

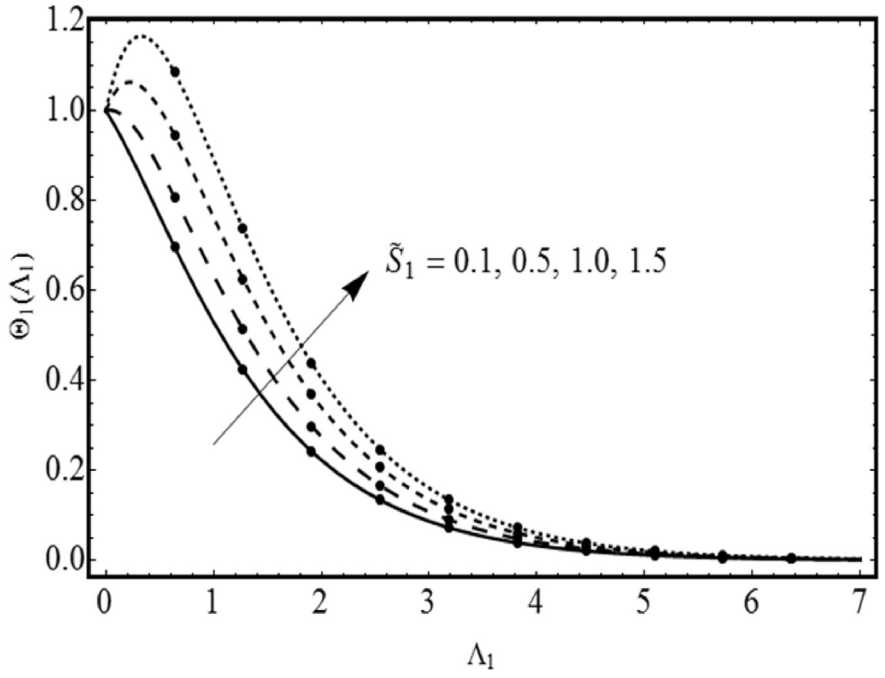

Fig. 14. Response of $\Theta_1(\Lambda_1)$ with $\tilde{S}_1$.

increased for larger $\tilde{N}_t$. Quick flows of fluid particles are established far away from cylindrical surface due to thermophoretic force caused by the temperature gradient. Due to which fluid that is more heated is shifted away from the surface and consequently as $\tilde{N}_t$ increases, the temperature $\Theta_1(\Lambda_1)$ inside the boundary layer upsurges.

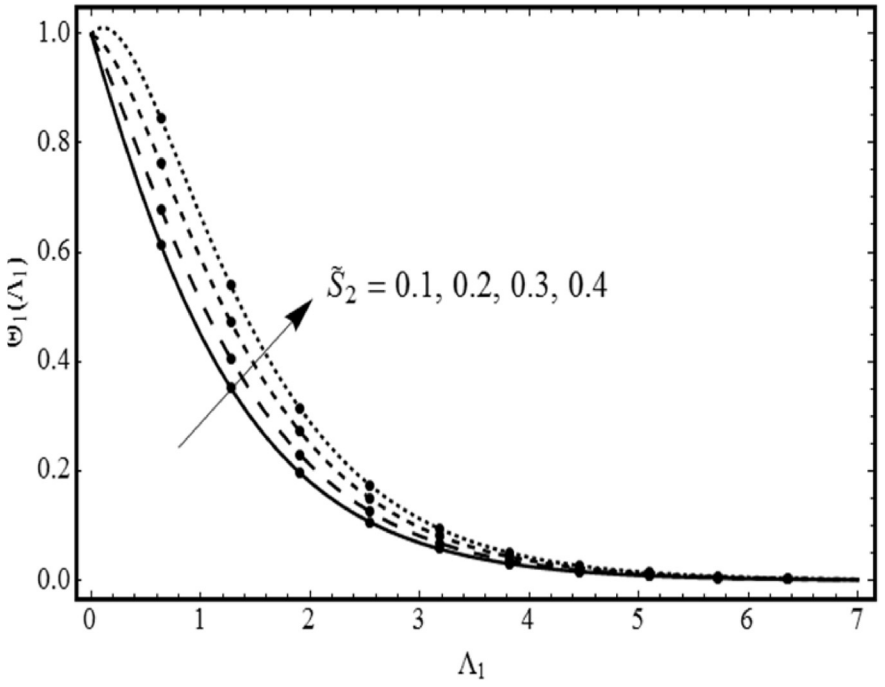

Fig. 15. Response of $\Theta_1(\Lambda_1)$ with $\tilde{S}_2$.

https://doi.org/10.1016/j.heliyon.2019.e01121

Fig. 13 reveals that temperature and thermal boundary layer thickness are diminished prominently for larger Pr. Since, Prandtl number is the ratio of momentum to thermal diffusivities. Increase in Prandtl number corresponds to weaker thermal diffusivity and stronger momentum diffusivity that consequently lowers the temperature profile. Fig. 14 is plotted to examine the temperature against distinct irregular heat parameter $\tilde{S}_1$. Here $\Theta_1(\Lambda_1)$ boost up for higher marks of $\tilde{S}_1$. In fact, it produces more thermal boundary thickness that becomes a source to generate heat. Hence enlargement in $\Theta_1(\Lambda_1)$ is pragmatic. Effect of space and temperature dependent heat source/sink parameters $\tilde{S}_1$ and $\tilde{S}_2$ on temperature $\Theta_1(\Lambda_1)$ are represented in Figs. 14 and 15. It is analyzed from these figures that more heat is produced for larger estimation of $\tilde{S}_1 > 0$ and $\tilde{S}_2 > 0$. Due to which temperature field enhances in both cases. Figs. 16, 17, 18, 19, 20, 21, 22, 23, 24, and 25 examine the influences of $\tilde{N}_t$, U_c, Sc, U_3, $\tilde{N}_b$, γ_1, E_o, $\tilde{\delta}_1$, $\tilde{P}_2$ and $\tilde{S}_1$ on $\Phi_1(\Lambda_1)$. Fig. 16 illustrates the effect of $\tilde{N}_t$ on $\Phi_1(\Lambda_1)$. Enhancing behavior of concentration $\Phi_1(\Lambda_1)$ and boundary thickness is found for increasing values of $\tilde{N}_t$. Existence of nanoparticles in fluid is in good agreement for the development of thermal conductivity. Such advanced thermal conductivity specifies the rise in concentration profile. Concentration distribution $\Phi_1(\Lambda_1)$ in frame of solutal relaxation time U_c is displayed in Fig. 17. Here concentration $\Phi_1(\Lambda_1)$ diminishes due to controlling influence of U_c. Impact of Schmidt number Sc on $\Phi_1(\Lambda_1)$ is disclosed through Fig. 18. Here $\Phi_1(\Lambda_1)$ is found to be decreasing function of Sc. Since, there exist an inverse relation between Schmidt number and mass diffusivity, therefore greater Sc leads to weaker mass diffusivity

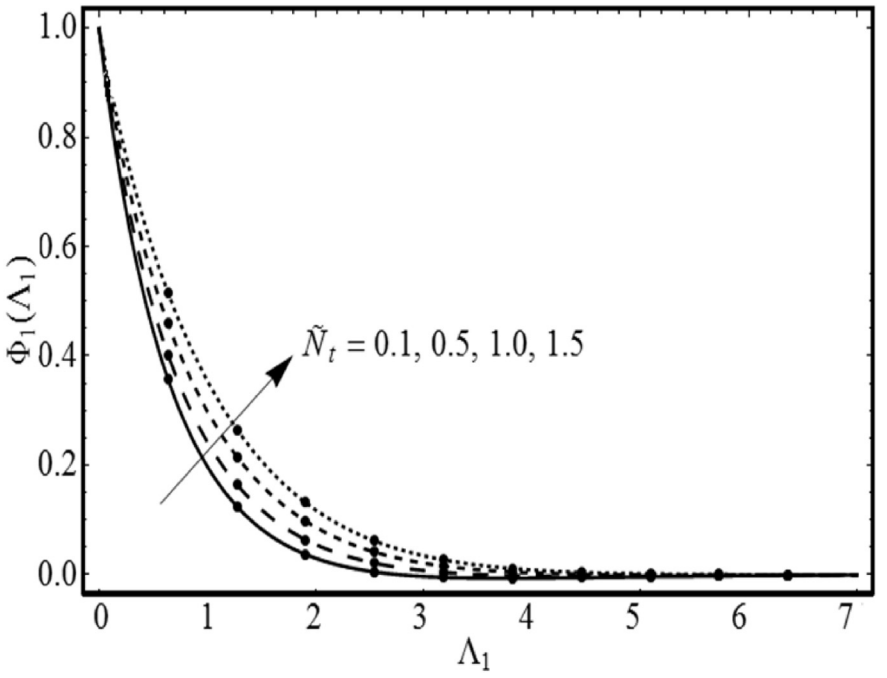

Fig. 16. Response of $\Phi_1(\Lambda_1)$ with $\tilde{N}_t$.

https://doi.org/10.1016/j.heliyon.2019.e01121

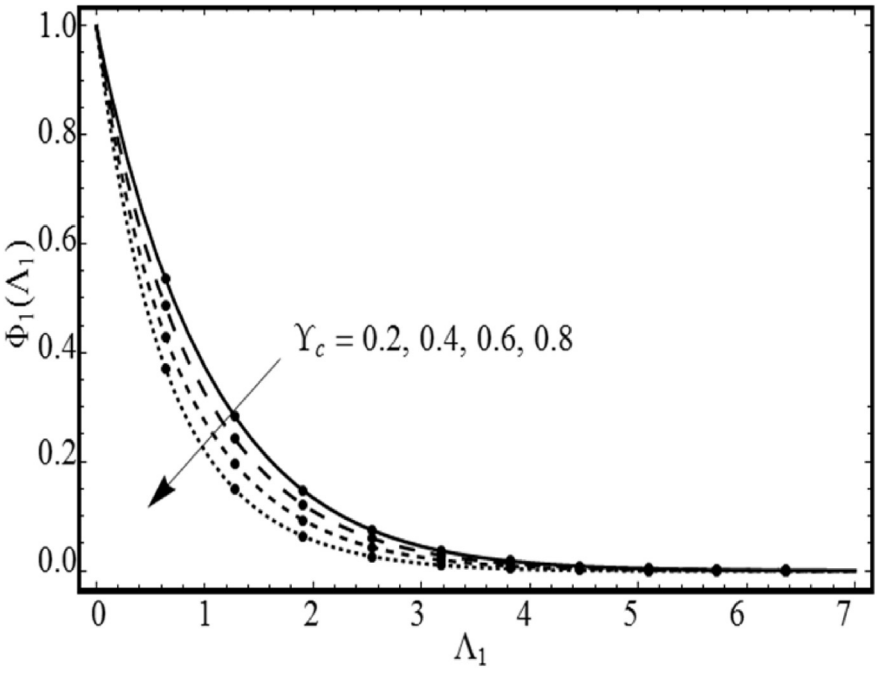

Fig. 17. Response of $\Phi_1(\Lambda_1)$ with U_c.

that is accountable to lower the concentration $\Phi_1(\Lambda_1)$ profile. Declining impact of concentration $\Phi_1(\Lambda_1)$ is observed for larger U_3 in Fig. 19. The growing nature of U_3 is responsible for rise in the expression $U_3(1+\tilde{\delta}_1\Theta_1)^{\widehat{p}}\, exp\big[-\frac{E_a}{1+\tilde{\delta}_1\Theta_1}\big]$.

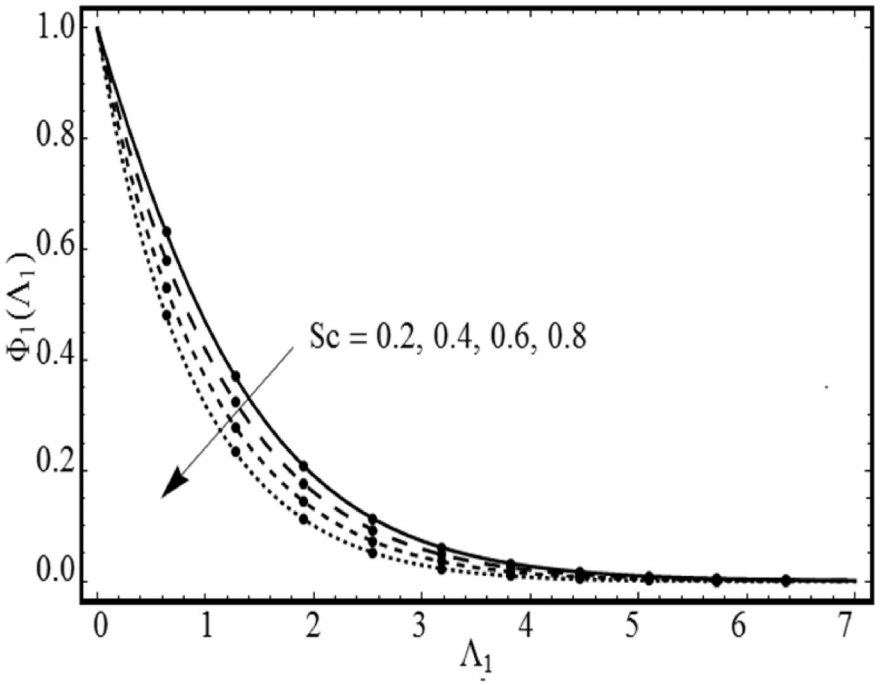

Fig. 18. Response of $\Phi_1(\Lambda_1)$ with Sc.

https://doi.org/10.1016/j.heliyon.2019.e01121

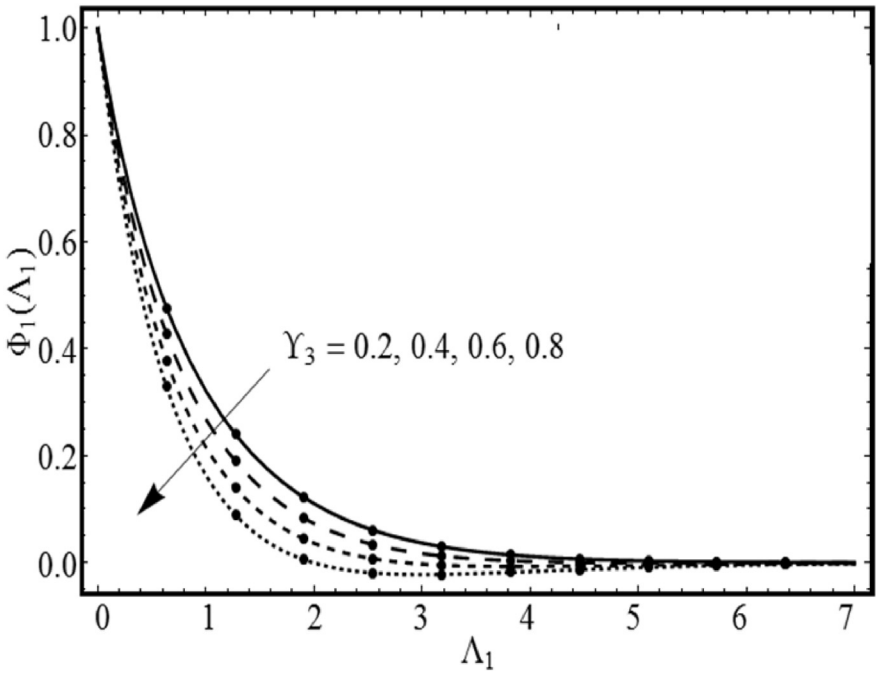

Fig. 19. Response of $\Phi_1(\Lambda_1)$ with U_3.

Physically, destructive rate of chemical reaction upsurges for greater estimation of U_3. This is used to dissolve/terminate the fluid specie more efficiently. Fig. 20 is remarked for the impact of $\tilde{N}_b$ on $\Phi_1(\Lambda_1)$. Enhancing conduct of $\Phi_1(\Lambda_1)$ and relevant boundary thickness is identified for greater $\tilde{N}_b$. An increase in $\tilde{N}_b$ corresponds

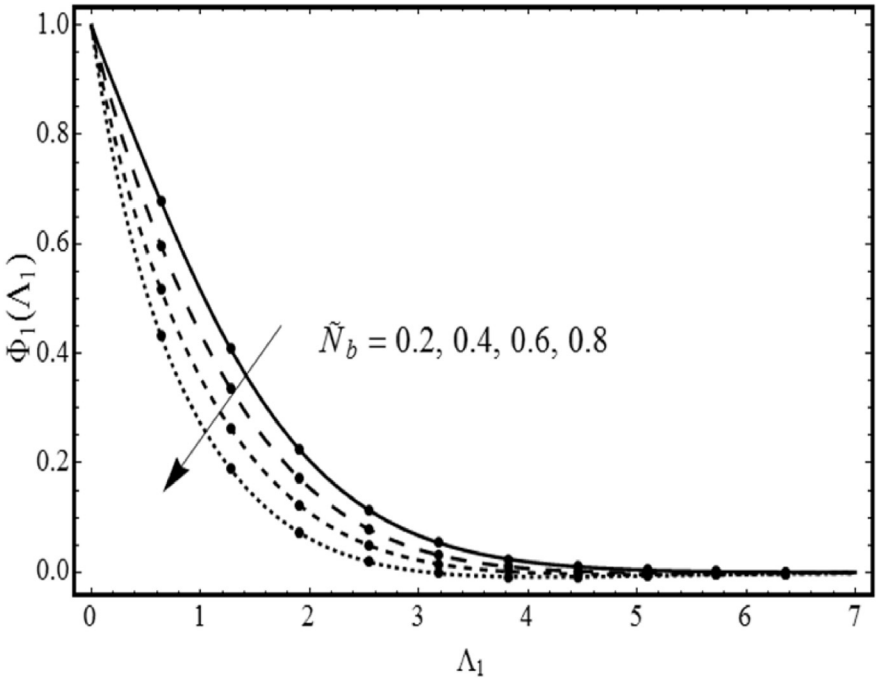

Fig. 20. Response of $\Phi_1(\Lambda_1)$ with $\tilde{N}_b$.

https://doi.org/10.1016/j.heliyon.2019.e01121

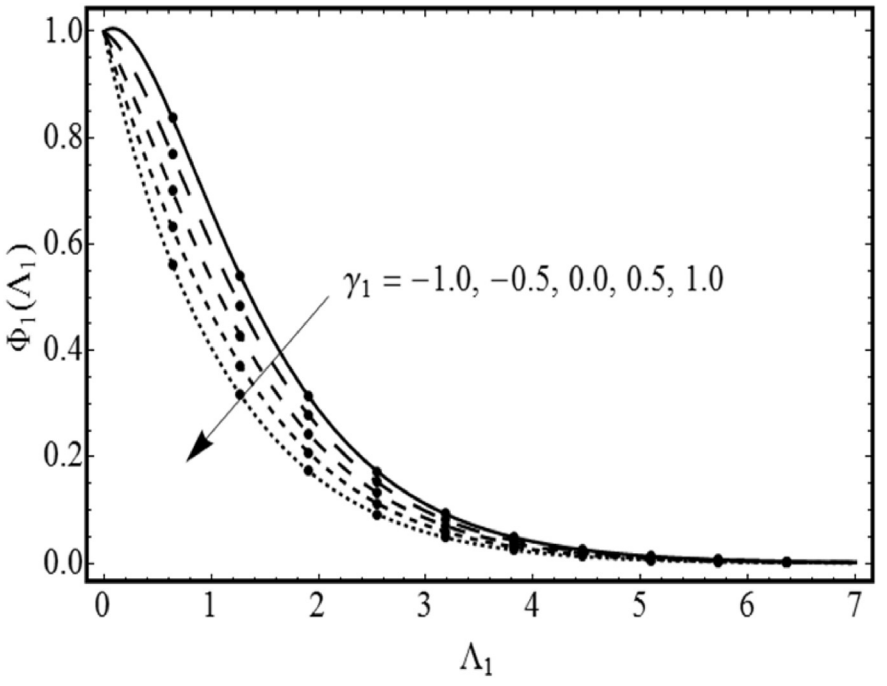

Fig. 21. Response of $\Phi_1(\Lambda_1)$ with γ_1.

to more collision among liquid particles due to which concentration $\Phi_1(\Lambda_1)$ reduces. Impact of generative/destructive chemical reaction γ_1 on concentration $\Phi_1(\Lambda_1)$ is outlined in Fig. 21. There is an increase in $\Phi_1(\Lambda_1)$ in vision of destructive chemical reaction variable $\gamma_1 > 0$. However, opposite trend is seen for

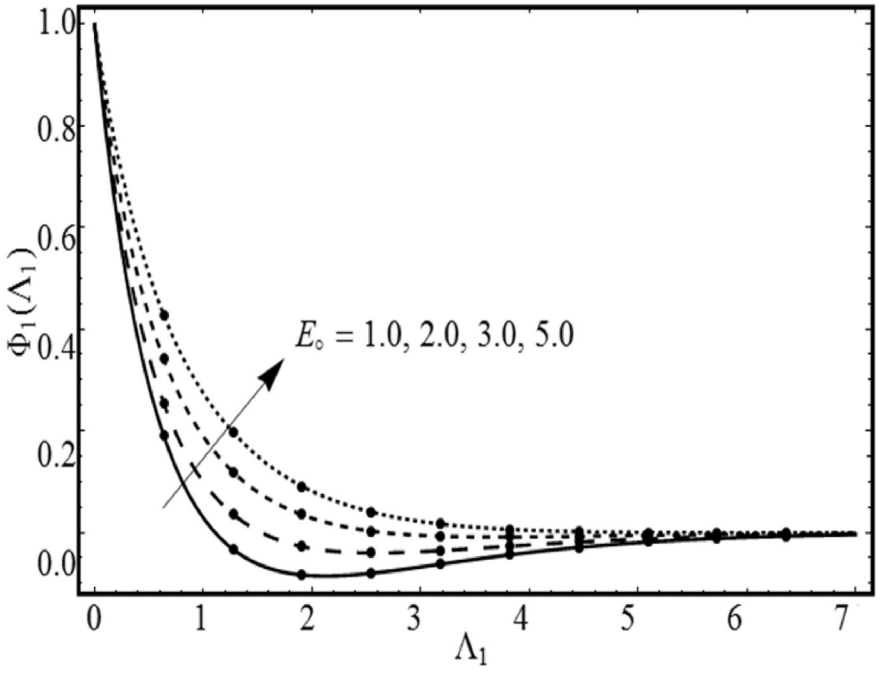

Fig. 22. Response of $\Phi_1(\Lambda_1)$ with E_o.

https://doi.org/10.1016/j.heliyon.2019.e01121

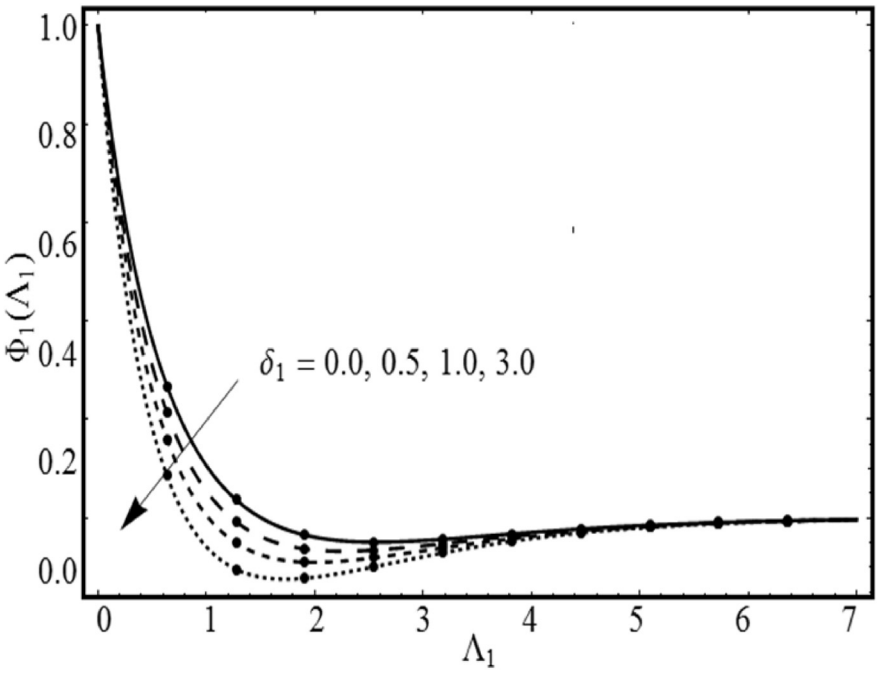

Fig. 23. Response of $\Phi_1(\Lambda_1)$ with $\tilde{\delta}_1$.

generative chemical reaction $\gamma_1 < 0$. Fig. 22 elucidates the increasing trend of activation energy E_o on nanoparticle concentration $\Phi_1(\Lambda_1)$. The modified Arrhenius function declines when E_o increases. This eventually endorses the generative chemical reaction due to which nanoparticle concentration rises. Fig. 23 shows the effect

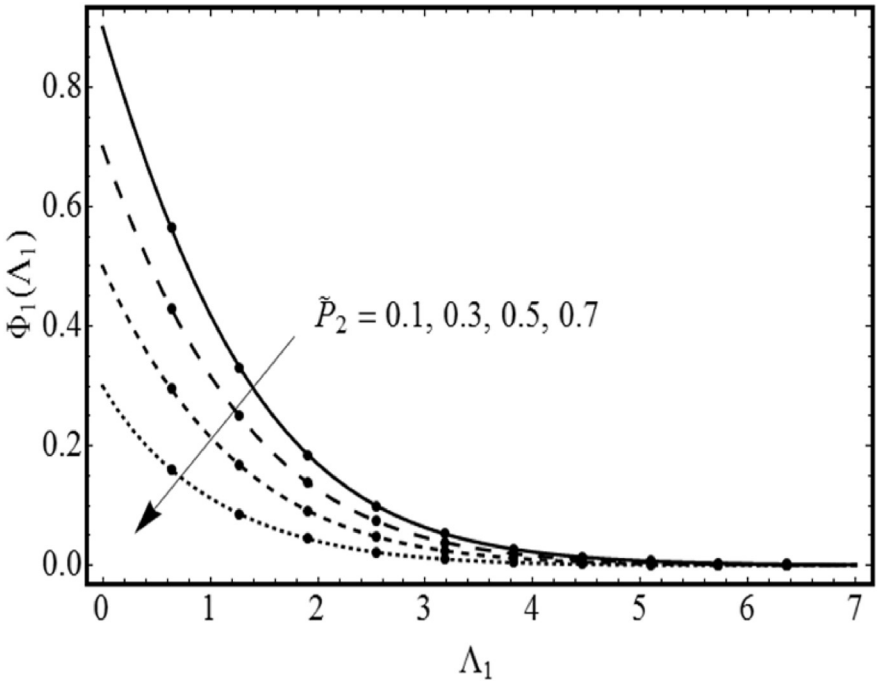

Fig. 24. Response of $\Phi_1(\Lambda_1)$ with $\tilde{P}_2$.

https://doi.org/10.1016/j.heliyon.2019.e01121

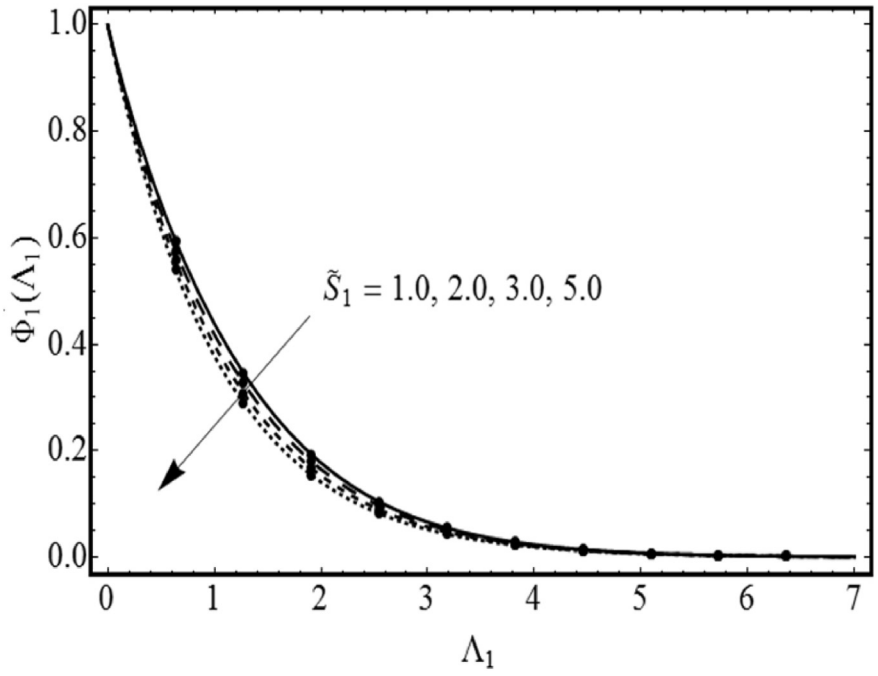

Fig. 25. Response of $\Phi_1(\Lambda_1)$ with $\tilde{S}_1$.

of concentration $\Phi_1(\Lambda_1)$ against temperature difference parameter $\tilde{\delta}_1$. Here declining role of $\tilde{\delta}_1$ on $\Phi_1(\Lambda_1)$ is observed. It specifies that relevant layer thickness rise when difference between surface and ambient temperature enlarges. Features of $\tilde{P}_2$ on $\Phi_1(\Lambda_1)$ are presented in Fig. 24. It is noticed that concentration $\Phi_1(\Lambda_1)$

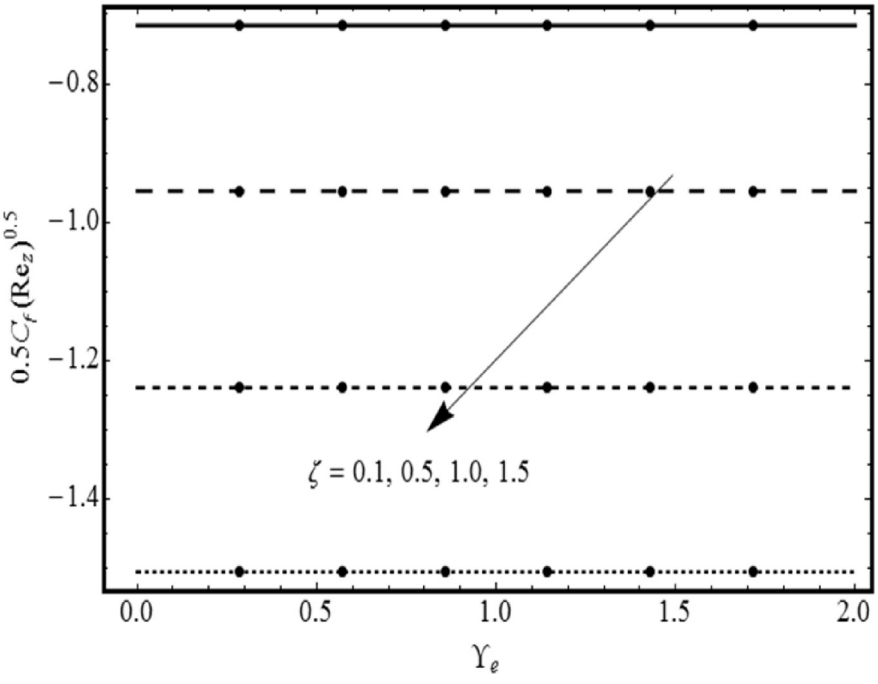

Fig. 26. Response of $0.5C_{\mathrm{F}}(Re_z)^{0.5}$ with ξ.

https://doi.org/10.1016/j.heliyon.2019.e01121

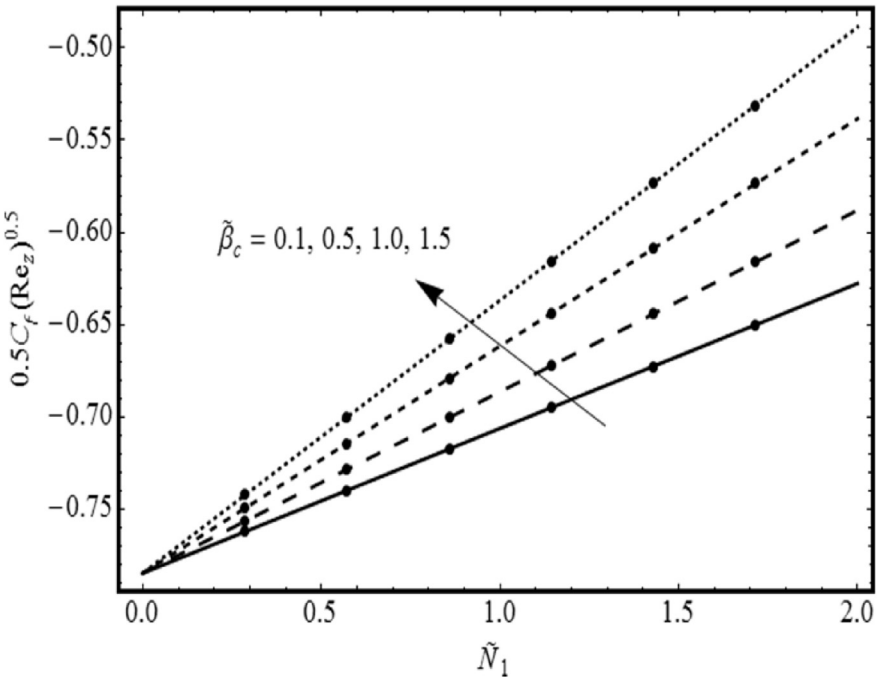

Fig. 27. Response of $0.5C_{\mathrm{F}}(Re_z)^{0.5}$ with $\tilde{\beta}_c$.

profile decreases for greater marks of P₂. Physically, it is because of difference between the surface and ambient concentration reduces for higher P_2. Consequently, $\Phi_1(\Lambda_1)$ decreases. Fig. 25 empowers us to decide that growth in $\tilde{S}_1$ leads to decline in concentration $\Phi_1(\Lambda_1)$ curve. Physically, increasing $\tilde{S}_1$ develops the thermal boundary layer thickness and hence it generates heat. That ultimately reduces fluid concentration $\Phi_1(\Lambda_1)$. Figs. 26 and 27 are prepared to examine the impact of emerging parameterson skin friction coefficient C_F. For greater estimation of ξ skin friction coefficient diminishes (see Fig. 26) while reverse behavior is observed for larger $\tilde{\beta}_c$ (see Fig. 27).

6. Conclusion

Here we have analyzed heat and mass transport phenomena for Maxwell nanofluid over a nonlinear stretched cylinder. The novel binary chemical reaction model is executed to describe the effect of activation energy for nonlinearly convective flow of viscoelastic fluid. The main findings are summarized as follows:

- $F'(\Lambda_1)$ decays for higher estimation of ξ and ϕ_1 while it boots up for $\widehat{\gamma}$, $\tilde{\beta}_t$ and $\tilde{\beta}_c$.
- Higher estimation of Deborah number declines the velocity $F'(\Lambda_1)$ profile.
- Temperature distribution declines for thermal relaxation time U_e and thermal stratification parameter $\tilde{P}_1$.

https://doi.org/10.1016/j.heliyon.2019.e01121

- Stratification variables $(\tilde{P}_1, \tilde{P}_2)$ diminish the temperature and concentration distributions.
- Concentration $\Phi_1(\Lambda_1)$ profile has reverse behavior for greater values of both $\tilde{N}_b$ and $\tilde{N}_t$.
- Higher Pr results in the reduction of $\Theta_1(\Lambda_1)$ profile while Nusselt number enhances.
- Nanoparticle concentration $\Phi_1(\Lambda_1)$ is directly proportional to the chemical reaction with activation energy.

Declarations

Author contribution statement

Misbah Ijaz: Analyzed and interpreted the data; Contributed analysis tools or data; Wrote the paper.

Muhammad Ayub: Conceived and designed the analysis; Analyzed and interpreted the data; Contributed analysis tools or data.

Funding statement

This research did not receive any specific grant from funding agencies in the public, commercial, or not-for-profit sectors.

Competing interest statement

The authors declare no conflict of interest.

Additional information

No additional information is available for this paper.

References

[1] M.S. Abel, J.V. Tawade, M.M. Nandeppanavar, MHD flow and heat transfer for the upper-convected Maxwell fluid over a stretching sheet, Meccanica 47 (2) (2011) 385−393.

[2] T. Hayat, M. Mustafa, S.A. Shehzad, S. Obaidat, Melting heat transfer in the stagnation-point flow of an upper-convected Maxwell (UCM) fluid past a stretching sheet, Int. J. Numer. Methods Fluid. 68 (2) (2011) 233−243.

https://doi.org/10.1016/j.heliyon.2019.e01121

[3] T. Hayat, S.A. Shehzad, H.H. Al-Sulami, S. Asghar, Influence of thermal stratification on the radiative flow of Maxwell fluid, J. Braz. Soc. Mech. Sci. Eng. 35 (4) (2013) 381–389.

[4] M. Mustafa, Cattaneo-Christov heat flux model for rotating flow and heat transfer of upper-convected Maxwell fluid, AIP Adv. 5 (4) (2015), 047109.

[5] L. Zheng, N. Liu, X. Zhang, Maxwell fluids unsteady mixed flow and radiation heat transfer over a stretching permeable plate with boundary slip and non-uniform heat source/sink, J. Heat Tran. 135 (3) (2013), 031705.

[6] T. Hayat, Z. Bashir, S. Qayyum, A. Alsaedi, Investigation of double diffusion Cattaneo-Christov model in mixed convection flow by variable thickness surface, Results Phys 7 (2017) 3873–3881.

[7] J.B.J. Fourier, Théorie analytique de la chaleur, Paris, 1822.

[8] A. Fick, Ueber diffusion, Annalen der Physik und Chemie 170 (1) (1855) 59–86.

[9] C. Cattaneo, Some aspects of diffusion theory, Atti Semin. Mat. Fis Univ. Modena Reggio Emilia 3 (1948) 83–101.

[10] C.I. Christov, On frame indifferent formulation of the Maxwell-Cattaneo model of finite speed heat conduction, Mech. Res. Commun. 36 (4) (2009) 481–486.

[11] S.A.M. Haddad, Thermal instability in Brinkman porous media with Cattaneo-Christov heat flux, Int. J. Heat Mass Tran. 68 (2014) 659–668.

[12] T. Hayat, T. Muhammad, A. Alsaedi, M. Mustafa, A comparative study for flow of viscoelastic fluids with Cattaneo-Christov heat flux, PLoS One 11 (5) (2016) e0155185.

[13] M. Waqas, T. Hayat, M. Farooq, S.A. Shehzad, A. Alsaedi, Cattaneo-Christov heat flux model for flow of variable thermal conductivity generalized Burgers fluid, J. Mol. Liq. 220 (2016) 642–648.

[14] T. Hayat, S. Qayyum, S. Shehzad, A. Sabir, A. Alsaedi, Cattaneo-Christov double-diffusion model for flow of Jeffrey fluid, J. Braz. Soc. Mech. Sci. Eng. 39 (12) (2017) 4965–4971.

[15] M. Waqas, M.I. Khan, T. Hayat, A. Alsaedi, On Cattaneo-Christov double diffusion impact for temperature-dependent conductivity of Powell-Eyring liquid, Chin. J. Phys. 55 (2017) 729–737.

https://doi.org/10.1016/j.heliyon.2019.e01121

[16] N. Ijaz, A. Zeeshan, M.M. Bhatti, R. Ellahi, Analytical study on liquid-solid particles interaction in the presence of heat and mass transfer through a wavy channel, J. Mol. Liq. 250 (2018) 80−87.

[17] T. Hayat, T. Ayub, T. Muhammad, A. Alsaedi, Flow of variable thermal conductivity Oldroyd-B fluid with generalized Fourier's and Fick's laws, J. Mol. Liq. 234 (2017) 09−17.

[18] A. Zeeshan, N. Shehzad, R. Ellahi, Analysis of activation energy in Couette-Poiseuille flow of nanofluid in the presence of chemical reaction and convective boundary conditions, Results Phys 8 (2018) 502−512.

[19] R. Ellahi, A. Zeeshan, N. Shehzad, Z.S. Alamri, Structural impact of Kerosene-Al2O3 nanoliquid on MHD Poiseuille flow with variable thermal conductivity: application of cooling process, J. Mol. Liq. 264 (2018) 607−615.

[20] M. Zubair, M. Ijaz, T. abbas, A. Riaz, Analysis of modified Fourier law in flow of ferromagnetic Powell-Eyring fluid considering two equal magnetic dipoles, Can. J. Phys. (2018).

[21] T. Hayat, T. Muhammad, On three-dimensional flow of couple stress fluid with Cattaneo-Christov heat flux, Chin. J. Phys. 55 (2017) 930−938.

[22] M. Ayub, T. Hayat, M. Waqas, M. Zubair, A. Alsaedi, Simulation of nonlinear convective thixotropic liquid with Cattaneo-Christov heat flux, Results Phys 8 (2018) 2812−2820.

[23] A. Majeed, A. Zeeshan, S.Z. Alamri, R. Ellahi, Heat transfer analysis in ferromagnetic viscoelastic fluid flow over a stretching sheet with suction, Neural Comput. Appl 30 (6) (2018) 1947−1955.

[24] E.M. Abo-Eldahab, M.A. El-Aziz, Blowing/suction effect on hydromagnetic heat transfer by mixed convection from an inclined continuously stretching surface with internal heat generation/absorption, Int. J. Therm. Sci. 43 (2004) 709−719.

[25] M.S. Abel, P.G. Siddheshwar, M.M. Nandeppanawar, Heat transfer in a viscoelastic boundary layer flow over a stretching sheet with viscous dissipation and non-uniform heat source, Int. J. Heat Mass Tran. 50 (2007) 960−966.

[26] M.S. Abel, N. Mahesha, Heat transfer in MHD viscoelastic fluid flow over a stretching sheet with variable thermal conductivity, non-uniform heat source and radiation, Appl. Math. Model. 32 (10) (2008) 1965−1983.

https://doi.org/10.1016/j.heliyon.2019.e01121

[27] K.A. Kumar, J.V.R. Reddy, V. Sugunamma, N. Sandeep, Magnetohydrodynamic Cattaneo-Christov flow past a cone and a wedge with variable heat source/sink, Alex. Eng. J. 57 (2018) 435–443.

[28] K. Mehmood, S. Hussain, M. Sagheer, Mixed convection flow with non-uniform heat source/sink in a doubly stratified magnetonanofluid, AIP Adv. 6 (2016), 065126.

[29] G. Kumaran, N. Sandeep, Thermophoresis and Brownian moment effects on parabolic flow of MHD Casson and Williamson fluids with cross diffusion, J. Mol. Liq. 233 (2017) 262–269.

[30] K.A. Kumar, J.V.R. Reddy, V. Sugunamma, N. Sandeep, MHD flow of chemically reacting Williamson fluid over a curved/flat surface with variable heat source/sink, Int. J. Fluid Mech. Res. 46 (2) (2018) 1–19.

[31] K.A. Kumar, V. Sugunamma, N. Sandeep, J.V.R. Reddy, Impact of Brownian motion and thermophoresis on bioconvective flow of nanoliquids past a variable thickness surface with slip effects, Heat Tran. Res. (2018), 025939.

[32] F. Hussain, R. Ellahi, A. Zeeshan, Mathematical models of electro magnetohydrodynamic multiphase flows synthesis with nano-sized Hafnium particles, Appl. Sci. 8 (2) (2018), 8020275.

[33] M. Hassan, M. Marin, A. Alsharif, R. Ellahi, Convective heat transfer flow of nanofluid in a porous medium over wavy surface, Phys. Lett. 382 (2018) 2749–2753.

[34] C. Truesdell, Sulle basi Della thermomeccanica, Accademia Nazionale del Lincei, Rendiconti della Classe di Scienze Fisiche, Matematiche e Naturali 22 (8) (1957) 33–38.

[35] C. Truesdell, Sulle basi della thermomeccanica, Accademia Nazionale del Lincei, Rendiconti della Classe di Scienze Fisiche 22 (1957) 158–166.

[36] A.R. Bestman, Natural convection boundary layer with suction and mass transfer in a porous medium, Int. J. Energy Res. 14 (4) (1990) 389–396.

[37] Kh. A. Maleque, Unsteady natural convection boundary layer heat and mass transfer flow with exothermic chemical reactions, J. Pure Appl. Maths 9 (1) (2013) 17–41.

[38] R. Kandasamy, K. Periasamy, K.K.S. Prabhu, Effects of chemical reaction, heat and mass transfer along a wedge with heat source and concentration in the presence of suction or injection, Int. J. Heat Mass Tran. 48 (2005) 1388–1394.

https://doi.org/10.1016/j.heliyon.2019.e01121

[39] O.D. Makinde, P.O. Olanrewaju, W.M. Charles, Unsteady convection with chemical reaction and radiative heat transfer past a flat porous plate moving through a binary mixture, Afr. Mat. 22 (2011) 65−78.

[40] M. Turkyilmazoglu, Some issues on HPM and HAM methods a convergence scheme, Math. Comput. Model. 53 (2011) 1929−1936.

[41] T. Hayat, M. Ijaz, M. Ayub, S. Qayyum, A. Alsaedi, Mixed convective stagnation point flow of nanofluid with Darcy-Fochheimer relation and partial slip, Results Phys 9 (2018) 771−778.

[42] T. Hayat, M. Rashid, A. Alsaedi, Three dimensional radiative flow of magnetite-nanofluid with homogeneous-heterogeneous reactions, Results Phys 8 (2018) 268−275.

[43] S.J. Liao, Beyond Perturbation: Introduction to Homotopy Analysis Method, Chapman and Hall/CRC Press, Boca Raton, 2003.

[44] T. Hayat, A. Aziz, T. Muhammad, A. Alsaedi, Model and comparative study for flow of viscoelastic nanofluids with Cattaneo-Christov double diffusion, PLoS One 12 (2017) e0168824.

[45] F. Mabood, S.M. Ibrahim, M.M. Rashidi, M.S. Shadloo, G. Lorenzini, Non-uniform heat source/sink and Soret effects on MHD non-Darcian convective flow past a stretching sheet in a micropolar fluid with radiation, Int. J. Heat Mass Tran. 93 (2016) 674−682.

[46] S. Qayyum, T. Hayat, A. Alsaedi, B. Ahmad, MHD nonlinear convective flow of thixotropic nanofluid with chemical reaction and Newtonian heat and mass conditions, Results Phys 7 (2017) 2124−2133.

[47] R. Cortell, Viscous flow and heat transfer over a nonlinearly stretching sheet, Appl. Math. Comput. 184 (2007) 864−873.

[48] A.M. Megahed, Variable fluid properties and variable heat flux effects on the flow and heat transfer in a non-Newtonian Maxwell fluid over an unsteady stretching sheet with slip velocity, Chin. Phys. B 22 (2013), 094701.

https://doi.org/10.1016/j.heliyon.2019.e01121